Title

The RAS GTPase RIT1 compromises mitotic fidelity through spindle assembly checkpoint suppression

Journal

Current Biology, 31(17)

ISSN

0960-9822

Authors

Cuevas-Navarro, Antonio
Van, Richard
Cheng, Alice
et al.

Publication Date

2021-09-01

DOI

10.1016/j.cub.2021.06.030

Peer reviewed

HHS Public Access

Author manuscript

Curr Biol. Author manuscript; available in PMC 2022 September 13.

Published in final edited form as:

Curr Biol. 2021 September 13; 31(17): 3915–3924.e9. doi:10.1016/j.cub.2021.06.030.

The RAS GTPase RIT1 compromises mitotic fidelity through spindle assembly checkpoint suppression

Antonio Cuevas-Navarro[1], **Richard Van**[1], **Alice Cheng**[1], **Anatoly Urisman**[2], **Pau Castel**[1,3,*], **Frank McCormick**[1,4,*]

[1]Helen Diller Family Comprehensive Cancer Center, University of California San Francisco, 1450 3rd St., San Francisco, CA 94158, USA

[2]Department of Pathology, University of California San Francisco, 513 Parnassus Ave., San Francisco, CA 94143, USA

[3]Present address: Department of Biochemistry and Molecular Pharmacology, New York University, 430 E 29th St., New York, NY 10016, USA

[4]Lead Contact

SUMMARY

The spindle assembly checkpoint (SAC) functions as a sensor of unattached kinetochores that delays mitotic progression into anaphase until proper chromosome segregation is guaranteed.[1,2] Disruptions to this safety mechanism lead to genomic instability and aneuploidy, which serve as the genetic cause of embryonic demise, congenital birth defects, intellectual disability, and cancer.[3,4] However, despite the understanding of the fundamental mechanisms that control the SAC, it remains unknown how signaling pathways directly interact with and regulate the mitotic checkpoint activity. In response to extracellular stimuli, a diverse network of signaling pathways involved in cell growth, survival, and differentiation are activated and this process is prominently regulated by the Ras family of small guanosine triphosphatases (GTPases).[5] Here we show that RIT1, a Ras-related GTPase that regulates cell survival and stress response,[6] is essential for timely progression through mitosis and proper chromosome segregation. RIT1 dissociates from the plasma membrane (PM) during mitosis and interacts directly with SAC proteins MAD2 and p31^{comet} in a process that is regulated by cyclin-dependent kinase 1 (CDK1) activity. Furthermore, pathogenic levels of RIT1 silence the SAC and accelerate transit through mitosis by sequestering MAD2 from the mitotic checkpoint complex (MCC). Moreover, SAC suppression by pathogenic RIT1 promotes chromosome segregation errors and aneuploidy. Our results highlight a unique

*Correspondence: Pau Castel, PhD Pau.castel@nyulangone.org; Frank McCormick, PhD Frank.mccormick@ucsf.edu.

AUTHOR CONTRIBUTIONS

A.C.-N., P.C. and F.M. conceived the project, supervised the research, and wrote the manuscript. A.C.-N. prepared the figures. A.C.-N. and R.V. performed the experiments. A.C. performed chromosome spread analysis. A.C. and A.U. performed MS sample preparation and analysis. All authors commented on and approved the manuscript.

DECLARATION OF INTERESTS

The authors declare no competing interests.

function of RIT1 compared to other Ras GTPases and elucidate a direct link between a signaling pathway and the SAC through a novel regulatory mechanism.

eTOC Blurb

Cuevas-Navarro *et al.* characterize a novel function of the Ras GTPase RIT1 as a negative regulator of the spindle assembly checkpoint (SAC) through its direct interaction with MAD2 and p31^{comet}. Moreover, disease-associated RIT1 mutations that evade protein turnover promote chomosome segregation errors and aneuploidy.

Graphical Abstract

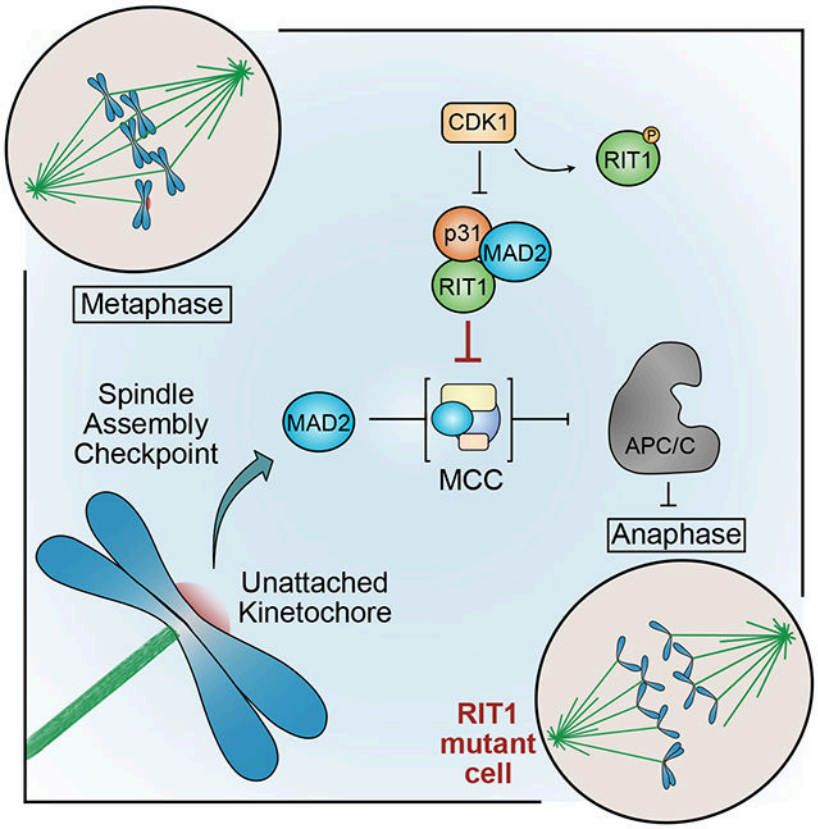

RESULTS AND DISCUSSION

RIT1 mutations have been identified as oncogenic drivers of lung adenocarcinoma and etiologic factors of Noonan syndrome.[7–9] RIT1 has a unique set of effector proteins but shares activation of the MAPK pathway with other Ras GTPases.[5,6,10] However, due to the lack of identified cognate GTPase activating protein or exchange factors, regulation of the RIT1 GTPase cycle remains unclear[6]. Nonetheless, RIT1 abundance and activity is regulated at the protein level through proteasomal degradation, a mechanism mediated by the adaptor protein LZTR1 and the E3 ubiquitin ligase Cullin 3 (CRL3^{LZTR1}).[11] While the role of RIT1 in Noonan syndrome is likely mediated by hyperactivation of the MAPK pathway, a pathognomonic sign of the disorder, its role in normal cells and in malignancies is less clear.

To characterize the RIT1 interactome, we performed an affinity purification-mass spectrometry screen (Figure 1A) that identified MAD2 (MAD2L1) and p31^{comet} (also known as MAD2L1-binding protein) as novel and selective RIT1 binding partners that do not interact with other Ras GTPases (Figures S1A and S1B). MAD2 participates in SAC signal amplification at unattached kinetochores which catalyze the formation of the MCC, comprised of MAD2, CDC20, BubR1, and Bub3.[1] In contrast, p31^{comet} binds MAD2 and silences MCC catalysis at unattached kinetochores and promotes the removal of MAD2 from the MCC.[12–16] MAD2 and p31^{comet} dimerization prompted us to assess whether RIT1 interacts with MAD2 and p31^{comet} directly.[17] Pulldown analysis revealed both interactions to be direct and independent on MAD2 and p31^{comet} dimerization (Figure 1B). Furthermore, the RIT1-MAD2 interaction is conserved in zebrafish and Drosophila (Figure 1C). To determine whether RIT1 binding to MAD2 or p31^{comet} is regulated by its GTPase cycle, we assessed binding to RIT1 loaded with GDP or GTPγS, a non-hydrolyzable GTP analog. This revealed that both interactions are independent of the guanosine nucleotide-loaded state of RIT1 (Figure 1D). Consistently, binding to MAD2 and p31^{comet} is not influenced by disease-associated RIT1 mutations (Figure S1C). These results suggest that the binding interface lies outside of RIT1's switch I and II domains which are sensitive to GDP/GTP binding, and, hence, MAD2 and p31^{comet} are not typical RIT1 effector proteins.

MAD2 and p31^{comet},s structural similarity highlighted potential binding competition for RIT1.[18,19] Thus, we used a competition binding assay in which titration of MAD2 WT or RQ, a dimerization and p31-binding deficient mutant, failed to suppress RIT1-p31^{comet} binding (Figure 1E).[20] These data support a non-competitive binding model. Notably, titration of MAD2 exerts a cooperativity effect on RIT1-p31^{comet} binding that relies on MAD2 and p31^{comet} dimerization. Binding cooperativity was further observed by gel filtration in which incubation of RIT1, MAD2, and p31^{comet} produced a high molecular-weight peak containing all three proteins, suggesting that they assemble into a multimeric complex *in vitro* (Figures S1D–S1I).

Due to the similarity between the RIT1 G-domain and that of other Ras GTPases, particularly its paralog RIT2, we hypothesized that RIT1's N-terminal or C-terminal extensions may mediate interaction with MAD2 and p31^{comet} (Figure 1F).[21] We analyzed RIT1 N- or C-terminal deletion mutants and demonstrated that the C-terminal domain is necessary and sufficient for MAD2 and p31^{comet} binding (Figures 1G, 1H, and S1J). Consecutive C-terminal truncations allowed us to identify residues 209-211 (SPF) as critical for MAD2 and p31^{comet} binding (Figures S1K and S1L) and, when mutated to corresponding RIT2 residues 207-209 (GSL), the interaction was significantly reduced (Figure 1I).

During interphase, RIT1's C-terminal tail mediates PM association.[22] However, when analyzing mitotic cells, we observed a diffuse cytoplasmic distribution of RIT1 as cells enter mitosis and as they progress through metaphase that is followed by rapid translocation to the PM during anaphase (Figures 2A and 2B). Consistently, a predominantly cytoplasmic distribution of endogenous RIT1 was detected in mitotic cell lysates (Figure 2C). In contrast, RIT1^{GSL} was not displaced from the PM (Figures S2A and S2B). These data indicate that diffusion of RIT1 between the PM and cytoplasm occurs during mitosis and may be

influenced by its association with MAD2 and/or p31^{comet}. Thus, we assessed binding of RIT1 to phospholipid-containing liposomes and noted that pre-incubation of RIT1 with MAD2, but not p31^{comet}, inhibited binding to phospholipid membranes (Figure S2C), suggesting mutual exclusivity between PM association and MAD2 binding.

Because our mass spectrometry revealed RIT1 C-terminal domain phosphorylation at S209 (Figure S2D), we hypothesized that a dynamic regulatory mechanism may control the interaction between RIT1 and MAD2 or p31^{comet}. Indeed, phospho-mimetic (S209D/E), but not phospho-deficient (S209A), mutations disrupted RIT1-MAD2/p31^{comet} binding (Figure 2D). Additionally, an antibody that detects RIT1 S209 phosphorylation (Figure S2E), showed that RIT1 phosphorylation is most abundant during mitosis (Figure 2E). To identify the kinase mediating phosphorylation of RIT1, we tested a panel of inhibitors against proline-directed serine/threonine kinases (Figure S2C).[23] Inhibition of CDK activity in prometaphase-arrested cells led to a reduction of RIT1 S209 phosphorylation. Furthermore, in a cell-free assay using mitotic cell extracts, CDK1 inhibition significantly reduced phosphorylation of recombinant RIT1 (Figure 2F). To determine whether RIT1 is a direct substrate of CDK1/CyclinB1, we performed *in vitro* kinase assays using recombinant proteins. RIT1 S209 phosphorylation by CDK1/CyclinB1 was detected by immunoblotting and confirmed by mass spectrometry (Figures 2G and 2H). These findings suggest CyclinB1/CDK1 phosphorylates RIT1 during mitosis, which coincides with the cell cycle pattern of CyclinB1 expression and CDK1 activity.[24] We propose that CDK1 regulates the association of RIT1 with MAD2 and p31^{comet} in a cell cycle-dependent manner. Since RIT1 S209 phosphorylation may also regulate its association with the PM, we evaluated the effect of S209A and S209D mutations on the subcellular distribution of RIT1; these had no noticeable effect on RIT1 during interphase (Figure S2G). However, in mitotic cells, RIT1^{S209A} remained at the PM throughout mitosis, while RIT1^{S209D} exhibited a diffuse cytoplasmic distribution but, unlike WT, failed to translocate to the PM during anaphase (Figures 2A, 2B and Figures S2H, S2I). Notably, RIT1^{S209A} constitutive PM association suggests that MAD2-binding capacity is not sufficient to extract RIT1 from the PM (Figure S2C). Together, these data suggest that CDK1 modulates both the subcellular distribution of RIT1 during mitosis and its association with MAD2/p31^{comet} (Figure S2J).

MAD2 and p31^{comet} regulate the duration of the SAC and, in turn, the duration of mitosis. This prompted us to examine whether RIT1, through its direct association with MAD2 and p31^{comet}, can influence the SAC. Depletion of RIT1 by RNAi or by CRISPR-mediated knockout resulted in prolonged mitotic progression (Figures 3A, S3A–S3E). Moreover, pharmacological inhibition of the SAC rescued the effect of RIT1 depletion, indicating that RIT1 affects mitosis in a SAC-dependent manner.[25] Furthermore, loss of RIT1 increased the rate of chromosome segregation errors (Figure 3B), suggesting that RIT1 is not only essential for timely progression through mitosis, but that dysregulation of RIT1 protein levels disrupt proper SAC function.

To further assess the effect of RIT1 on the SAC, we knocked out LZTR1 or expressed RIT1^{M90I}, a pathogenic variant that is insensitive to CRL3^{LZTR1}-mediated protein degradation, resulting in increased RIT1 expression levels (Figures S3F and S3G).[11] Loss of LZTR1 or RIT1^{M90I} expression accelerated the rate of mitotic progression in

asynchronously growing cells, an effect that relied on the release of RIT1 from the PM (Figures 3C, S3H, S3I). Similarly, overexpression of RIT1 WT or M90I partially overrode the pharmacologically-induced SAC response (Figures 3D and S3J). Importantly, abolishing MAD2 and p31^{comet} binding using RIT1 phospho-mimetic mutants rescued suppression of the SAC mediated by RIT1^{M90I} (Figures S3K and S3L). Of note, the M90I/S209A mutant retained the ability to suppress the SAC despite being insensitive to CDK1/Cyclin B-mediated regulation, suggesting that at pathogenic expression levels, sufficient RIT1 molecules reside in the cytoplasm to interact with MAD2 and p31^{comet}. We did not observe a discernible difference in basal MAPK activation between these mutants, ruling out the possibility that the rescue effect exhibited by these mutants was due to altered MAPK signaling (Figure S3N). To evaluate the role of RIT1's GTPase activity on SAC suppression, we generated an inactive, GDP-bound mutant (M90I/S35N) that retained the ability to accelerate the rate of mitotic progression (Figure 3E and 3F). These data suggest that the G-domain, which is dispensable for MAD2/p31^{comet} binding, may not play a direct role in SAC silencing. To further evaluate this hypothesis, we generated a chimeric EGFP-RIT1 C-terminal tail fusion protein whose overexpression was sufficient to suppress the SAC (Figure S3N).

A weakened SAC may allow precocious anaphase entry that results in chromosome instability and missegregation.[26–30] Therefore, we examined whether RIT1-mediated suppression of the SAC promotes chromosome segregation errors in HCT-116, a cancer cell line with a near diploid karyotype that exhibits low chromosomal instability.[31] Ectopic expression of RIT1^{M90I} significantly increased the rate of mitotic errors, including lagging and bridging chromosomes, in a MAD2- and p31^{comet}-binding dependent manner (Figures 3G and S3O). Consequently, we observed an increased rate of aneuploidy in cells expressing RIT1^{M90I}, but not in cells expressing the mutant that is unable to bind MAD2/p31^{comet} (Figures 3H and S3P). These results demonstrate that increased levels of RIT1 lead to compromised mitotic fidelity as a result of direct interaction with MAD2 and p31^{comet}.

SAC signaling is tightly regulated and amplified by the catalyzed conversion of MAD2 from its open (O-MAD2) to its closed conformational state (C-MAD2) upon binding MAD1 at unattached kinetochores.[18,32,33] The conformational change in MAD2 primes its association with CDC20.[34,35] To directly test whether RIT1 inhibits the association of MAD2 with CDC20 or MAD1, we performed competitive pulldown assays to test mutual exclusivity between RIT1-MAD2 and MAD2-CDC20/MAD1 binding (Figures 4A and 4B). MAD2 binding peptide 1 (MBP1), a high-affinity synthetic peptide that mimics the MAD2 interaction motifs (MIM) of CDC20 and MAD1, abolished MAD2-RIT1 binding.[35] Conversely, titration of full-length RIT1 reduced binding of MAD2 to CDC20 MIM beads,[36] suggesting that RIT1 competes with CDC20 and MAD1 for MAD2 binding. However, since binding to MBP1 or CDC20$^{111\text{-}138}$ drives the conversion of O-MAD2 to C-MAD2, an alternative explanation may be that RIT1 preferentially binds to O-MAD2.[35] To distinguish between these two models, we assessed the binding of RIT1 with O- or C-state stabilized MAD2 mutants (Figure 4C).[18] C-MAD2 mutants retained their interaction to RIT1, whereas O-MAD2 mutants failed to bind RIT1, except MAD2^{LL} that can adopt a closed conformation state in the presence of MIM ligand.[34] Furthermore, expression of a MAD2 phosphomimetic mutant in cells that adopts the O-MAD2 conformer fails

to bind RIT1 (Figure S4A).[37] These results demonstrate that RIT1 exhibits preferential binding to C-MAD2 over O-MAD2, potentially stabilizing the closed conformer; moreover, RIT1 directly competes with CDC20 and MAD1 for MAD2 binding *in vitro*. We posit that RIT1 and CDC20/MAD1 may compete for the same interface on MAD2, which would predict that RIT1 binding promotes the conversion of O-MAD2 to C-MAD2.[35,38] To test this hypothesis, we incubated MAD2 protein with excess RIT1 C-terminal tail peptide and separated by gel filtration (Figure 4D). In the presence of excess RIT1 peptide, MAD2 protein fails to dimerize, similar to previous reports in which excess CDC20 peptide disrupted O-MAD2:C-MAD2 dimers by saturating all molecules into their closed conformational state.[32,39] In contrast, incubation with RIT1 S209 phosphorylated peptide did not disrupt the formation of MAD2 dimers (Figure 2D). RIT1 preferential binding to C-MAD2 and dimerization of p31^{comet} with C-MAD2 suggests that their oligomerization produces a RIT1-C-MAD2-p31^{comet} complex and, hence, would explain the increased RIT1-p31^{comet} affinity observed in the presence of MAD2 (Figure 1E).

Our biochemical analyses support a model of RIT1-mediated SAC inhibition that involves the sequestration of MAD2 away from MAD1 and/or CDC20 complexes. To test this model in a cellular context, we first analyzed MAD2 recruitment to unattached kinetochores and observed no measurable differences under RIT1 depletion or ectopic RIT1^{M90I} expression (Figures S4B–S4E), suggesting that RIT1 may regulate the SAC downstream of kinetochores. Thus, we examined MAD2-CDC20 binding in cells by interrogating MCC integrity under nocodazole washout. RIT1 depletion did not affect MCC disassembly (Figures S4F and S4G), potentially due to compensatory p31^{comet} silencing.[16,40] However, RIT1^{M90I} significantly reduced MAD2-CDC20 and BubR1-CDC20 interactions (Figures 4E and 4F). These data suggest that pathogenic RIT1 protein levels hinder MCC integrity and are in line with the model that RIT1 sequesters MAD2 from CDC20 and promotes MCC disassembly.

To investigate the effect of RIT1 on MAD2 and CDC20 binding in the presence of p31^{comet}, we conducted competitive pulldown assays. Consistent with the cooperativity effect exhibited by the RIT1-MAD2-p31^{comet} complex, the addition of p31^{comet} enhanced RIT1-mediated inhibition of MAD2-CDC20 binding (Figures S4H and S4I). Furthermore, RIT1 and p31^{comet} cooperation was dependent on MAD2-p31^{comet} dimerization. These results suggest that RIT1 may cooperate with p31^{comet} to extract MAD2 from the MCC and promote its disassembly.

Regulation of mitotic progression by the SAC is achieved through inhibition of the anaphase-promoting complex/cyclosome (APC/C) by the MCC.[41] We reasoned that RIT1 inhibition of MAD2-CDC20 association may promote APC/C activity. Therefore, we measured *in vitro* ubiquitination and degradation of APC/C substrates CyclinB1 and Securin in MCC active mitotic cell extracts isolated from RIT1 knockout cells.[42] Supplementing these extracts with recombinant RIT1 increased ubiquitination and degradation of CyclinB1 and Securin, suggesting increased APC/C activity, likely due to relieved MCC inhibition (Figures 4G, S4J–S4K). To evaluate APC/C activity *in vivo*, we measured degradation of fluorescently-labeled CyclinB1 during mitosis. Consistent with delayed mitotic progression (Figure 3A), RIT1-depleted cells exhibited delayed CyclinB1 degradation (Figure 4H).

Moreover, expression of RIT1^{M90I} accelerated CyclinB1 degradation under normal cell growth (Figure 4I); however, its effect on CyclinB1 degradation was abolished under pharmacologically-induced mitotic arrest (Figure S4M), suggesting that pathogenic levels of RIT1 cannot silence a hyperactive SAC response.

Altogether, our findings demonstrate that RIT1 regulates mitotic fidelity through a direct complex formation with MAD2/p31^{comet} that results in suppression of the SAC response. CDK1/CyclinB1 regulates RIT1's dissociation from the PM during mitosis, a process necessary for RIT1-mediated SAC suppression, and inhibits the formation of RIT1-MAD2-p31^{comet} complexes. CDK1 orchestrates mitotic progression through phosphorylation of various substrates and is most active during prometaphase.[43] In line with this, we can deduce that CDK1/CyclinB1 modulates RIT1-mediated SAC inhibition during the early stages of mitosis when SAC signaling is essential for proper chromosome segregation.[1] Pathogenic RIT1 levels suppress SAC signaling and we speculate that overabundant RIT1 escapes adequate CDK1 phosphorylation achieved under physiological RIT1 levels, resulting in a weakened SAC response. To fully understand the properties of RIT1 as an oncogenic driver, it will be paramount to investigate whether SAC silencing contributes to the pathogenesis of *de novo* RIT1 mutations that compromise RIT1 degradation, as this may provide an avenue for therapeutic intervention.[11] It is tempting to speculate that RIT1 may provide a direct link between SAC regulation and RIT1 effector pathways involved in cell survival and stress response.[6] Moreover, one can postulate that the RIT1-SAC signaling axis may have evolved as a mechanism that modulates SAC activity in response to mitogenic and stress signals. While previous reports have implicated pathogenic Ras GTPase signaling with genomic instability,[44–46] our results show a direct link between the SAC and a member of the Ras GTPase family, providing a novel example of the evolutionary adaptation of a signaling molecule for the regulation of a unique but critical cellular pathway.

STAR★METHODS

RESOURCE AVAILABILITY

Lead Contact—Further information and requests for resources and reagents should be directed to and will be fulfilled by the Lead Contact, Frank McCormick (Frank.mccormcik@ucsf.edu).

Meterial Availability—All unique/stable reagents generated in this study are available from the Lead Contact with a completed Materials Transfer Agreement.

Data and Code Availability

- All data reported in this paper will be shared by the lead contact upon request.
- This paper does not report original code.
- Any additional information required to reanalyze the data reported in this work paper is available from the Lead Contact upon request.

EXPERIMENTAL MODEL AND SUBJECT DETAILS

Cells and culture conditions—HEK-293T, HeLa, U2-OS, HCT-116, and hTERT RPE-1 cells were obtained from the American Type Culture Collection (ATCC). HEK-293T, HeLa and U2-OS cells were cultured in Dulbecco's modified Eagle's medium (DMEM) supplemented with 10% Fetal Bovine Serum (FBS). hTERT RPE-1 cells were cultured in DMEM/F12 medium supplemented with 10% FBS. Cells were grown in a humidified incubator with 5% CO2 at 37 °C. Validation procedures are as described by the manufacturer. Cell lines were regularly tested and verified to be mycoplasma negative using MycoAlert PLUS Mycoplasma Detection Kit (Lonza).

METHOD DETAILS

Reagents, antibodies, and immunoblotting—Nocodazole, Reversine, Dinaciclib, RO-3306, JNK-IN-8, CHIR-99021, TG003, Losmapimod, and Trametinib were purchased from Selleckchem. MG132, Thymidine, ATP, phospho-creatine, GDP and GTPγS were purchased from Sigma-Aldrich. RIT1 (202-216), pS209 RIT1 (202-216), MBP1 (SWYSYPPPQRAV) and control (SYWPQRAPPSVY) peptides were obtained from GenScript. Antibodies against p-ERK (4370; 1:1000), ERK1/2 (4696; 1:2000), p-MEK (9154; 1:1000), MEK1/2 (4694; 1:1000), Cyclin B1 (4135, 1:1000), HA (3724, 1:1000), FLAG (14793; 1:1000), GST (2625; 1:1000), and (K/H)pSP (9477, 1:1000) were obtained from Cell Signal Technology. Antibodies recognizing Securin (PTTG) (sc-56207; 1:250), MAD2 (sc-47747; 1:250) and GST (sc-138; 1:1000) were obtained from Santa Cruz Biotechnology. RIT1 antibody (ab53720; 1:1000) was from Abcam. $p31^{comet}$ antibody (MABE451; 1:500) was from EMD Millipore. MAD2 antibody (A300-301A; 1:1000) was from Bethyl Laboratories. βActin (A2228; 1:10000), α-Tubulin (T6199; 1:5000), FLAG (F1804; 1:2000) and His_6 (05-949; 1:1000) antibodies were purchased from Sigma-Aldrich. Whole cell lysates were prepared using RIPA Buffer (50 mM Tris-HCl (pH 8.0), 150 mM NaCl, 0.5% Deoxycholate, 0.1% SDS, 1% IGEPAL CA-630) supplemented with protease and phosphatase inhibitor cocktails (Sigma-Aldrich). 20-30 μg of total protein was loaded per well of pre-casted NuPAGE gels (Life Technologies). For immunoblot detection, samples were separated by SDS-PAGE and transferred onto nitrocellulose membranes. Membranes were blocked using 5% skimmed milk in TBST buffer for 1 hour and incubated with appropriate primary antibodies overnight. Detection was performed using secondary antibodies conjugated to DyLight680 (611-144-002; 1:10,000) or DyLight800 (610-145-002; 1:10,000) (Rockland), and visualized with a LI-COR Odyssey infrared scanner.

Plasmids, cloning and transfection—All RIT1 mutations used in this paper were generated by standard PCR-based mutagenesis in the pDONR223-RIT1 template. These included ΔN, ΔC (and all C-terminal truncations), GSL, S209A, S209D, S209E, A57G, A77P, F82L, M90I, S35N,[52] and Q79L.[53] Mutagenesis primer sequences are available upon request. RIT2 (Isoform 1, NM_002930.4), RIT1 (RIT2 Ct) chimera, and mNeonGreen-RIT1 were synthesized as a gene block and cloned into pDONR221 (Invitrogen) using BP reaction. LR Gateway cloning yielded mammalian expression vectors with indicated tags. For N-terminal GST-tagged proteins, entry clones were cloned into pDEST27 destination vector (Invitrogen). For FLAG-tagged proteins, entry clones were cloned by multisite

gateway cloning into pDEST302, pDEST663 or pDEST686 (a gift from Dominic Esposito, Frederick National Lab), and designed to express N-terminal 3xFLAG tag fusion proteins driven by an EF1a promoter.[54] Empty vector (EV) plasmid controls were generated using a gateway recombination cassette containing a stop codon followed by an untranslated stuffer sequence. The GST-tagged Ras Family GTPases panel was cloned in the pDEST27 vector and was previously described.[10] MAD2 cDNA (NM_002358.3) was purchased from GeneCopoeia as a Gateway entry clone and was recombined into pcDNA3-HA destination vector to be expressed an N-terminal HA-tagged fusion protein. MAD2 S195A and S195D were generated by PCR-based mutagenesis. All plasmid transfections in this study were performed using JetPRIME transfection reagent (Polyplus Transfection) according to manufacturer's instructions.

Constructs used for bacterial expression were generated from as follows: a gene block containing *E. coli* codon-optimized human RIT1 (a.a.1-219), with an N-terminal TEV cleavage site followed by a FLAG-tag, was cloned into pDONR221 (Invitrogen). Similarly, gene blocks encoding *E. coli* codon-optimized human MAD2 (1-205) and $p31^{comet}$ (1-274), both with an N-terminal TEV cleavage site, were synthesized and cloned into pDONR221. MAD2 R133E/Q134A (RQ); ΔC (1-195); Loop-less (LL), in which residues 109-117 are replaced with a Gly-Ser-Gly linker; V193N; L13A; and ΔN15 (16-195); and $p31^{comet}$ΔN were generated by standard PCR-based mutagenesis.[18] $p31^{comet}$ΔN (50-274) was generated to enhance protein stability through deletion of its non-conserved and disordered N-terminal fragment.[19] Zebrafish (*Danio rerio*) and Fruit fly (*Drosophila melanogaster*) MAD2 and RIT1 orthologs were synthesized as *E. coli* codon-optimized gene blocks and cloned into pDONR221. RGL3-RBD (604-703) was synthesized as an *E. coli* codon-optimized gene block and subcloned into pGEX-6P-3 at EcoRI and XhoI restriction sites. All plasmids were verified by Sanger sequencing.

RNA interference—The short interfering RNAs (siRNAs) used in this study are siRIT1 (SMARTpool: ON-TARGETplus RIT1, Horizon) and siNTC (ON-TARGETplus Non-targeting Control Pool, D-001810-10-05, Horizon). Cells were transfected with siRNAs using Lipofectamine RNAi Max Transfection Reagent (Life Technologies) according to manufacturer's instructions.

Generation of CRISPR/Cas9-mediated knockout cells—RIT1 knockout (KO) clones were generated using two sgRNA targeting exon 2 of RIT1: sgRIT1-1: GATTCTGGAACTCGCCCAGT and sgRIT1-2: GGAGTACAAACTAGTGATGC. LZTR1 KO clones were generated sgRNA previously described; sgLZTR1-1: AGTCTTTCACATCGAACCGC and sgLZTR1-2: CTTTACTCAGGGGGTTACAC. Briefly, Parental cells were transiently transfected with plasmid encoding an individual sgRNA, SpCas9, and EGFP (PX458, Addgene, plasmid #48138). 48 h post-transfection, GFP+ cells were single-cell sorted into 96-well plates using a SONY SH800 FACS. Clones were expanded and KO clones were validated by Sanger sequencing and Western blot analysis.

Lentiviral transduction—Lentivirus was produced by co-transfection of HEK-293T cells with a lentiviral vector and the packaging plasmids psPAX2 (Addgene, plasmid #12260) and pMD.2G (Addgene, plasmid #12259) at a ratio of 1.25:1.0:0.25. The supernatant

was collected 72 hours post-transfection and filtered through a 0.45 μm filter. Cells were transduced with lentiviral-containing supernatant supplemented with 0.8 μg/ml polybrene (Sigma-Aldrich). Stably transduced cells were selected with appropriate antibiotic and maintained in media containing 50% antibiotic used during selection.

Bacterial protein expression and purification—Full-length recombinant RIT1 protein was obtained by gateway cloning pDONR-TEV-FLAG-RIT1 WT or S209A into pDEST566 (Addgene, plasmid #11517) containing an N-terminal hexahistidine-maltose binding protein (His_6-MBP) tag. Expression constructs were transformed into the *E. coli* strain BL21(DE3) (New England Biolabs). Protein expression was induced in cultures at OD_{600} between 0.4-0.6 with 200 μM Isopropyl β-D-1-thiogalactopyranoside (IPTG) (Sigma-Aldrich) for 14-16 h at 18°C. Cells were lysed by sonication in 100 mM Sodium phosphate (pH 6.0), 300 mM NaCl, 10 mM $MgCl_2$, 5% glycerol, 2 mM DTT, 1 mg/ml DNAse I, 0.2 mg/ml lysozyme, 30 mM imidazole and protease inhibitor cocktail (Sigma-Aldrich, P8849). After clearing, the lysate was loaded on a HisTrap FF metal chelating column (Cytiva Life Sciences) equilibrated in 100 mM Sodium phosphate (pH 6.0), 300 mM NaCl, 10 mM $MgCl_2$, 5% glycerol, 30 mM imidazole. Bound proteins were eluted with 300 mM imidazole. Fractions containing RIT1 were pooled and dialyzed overnight in the presence of TEV-protease (Sigma-Aldrich). Cleaved protein was recovered by subtractive purification, concentrated by ultrafiltration, and further separated by size exclusion chromatography (SEC) on a Superdex-75 column (Cytiva Life Sciences) equilibrated in 100 mM Sodium phosphate (pH 6.0), 300 mM NaCl, 10 mM $MgCl_2$, 5% glycerol, 0.5 mM TCEP. RIT1 containing fractions were pooled, concentrated and frozen in liquid nitrogen. The entire purification scheme was carried out at 4°C. Recombinant $p31^{comet}$ WT and ΔN protein were expressed and purified analogously but with the use of 50 mM Tris-HCl (pH 8.0) buffer without $MgCl_2$.

Recombinant MAD2 WT and RQ were expressed from pDEST527 (Addgene, plasmid #11518) containing an N-terminal hexahistidine-tag in BL21(DE3) following the same conditions described above in 50 mM Tris-HCl (pH 8.0) buffer without $MgCl_2$. After subtractive purification, TEV-cleaved MAD2 protein was dialyzed overnight in anion-exchange (AE) buffer (10 mM Tris-HCl (pH 8.0), 30 mM NaCl, 5% glycerol and 1 mM DTT). MAD2 was loaded onto an AE Resource-Q column (Cytiva Life Sciences) equilibrated in AE Buffer. The protein was eluted using a NaCl gradient, concentrated and flash-frozen in liquid nitrogen.

Recombinant GST-tagged proteins were expressed from a pGEX-6 plasmid transformed into BL21 (DE3) cells. Expression was induced with 0.2 mM IPTG for 14-16 h at 18°C. Cells were lysed by sonication in 50 mM Tris-HCl (pH 8.0), 300 mM NaCl, 5% glycerol, 1 mM DTT. Proteins were immobilized on Glutathione sepharose 4B beads (Cytiva Life Sciences), washed extensively, and stored as a 50% glycerol bead suspension at −20°C.

Immunoprecipitation and GST pulldown assays—GST pulldown assays with recombinant proteins were performed by diluting indicated proteins in 500 μl of pulldown buffer (10 mM Tris-HCl (pH 8.0), 150 mM NaCl, 0.1% IGEPAL CA-630, 10% glycerol) and 20 μl of Glutathione sepharose 4B beads (Cytiva Life Sciences) for 1 h at 4°C with

end over end rotation. Beads were rinsed three times with pulldown buffer and resuspended in LDS sample buffer (Life Science Technologies) for immunoblot or Coomassie staining of SDS-PAGE gels. For nucleotide loading, RIT1 was incubated in 100 μl GTPase loading buffer (20 mM Tris 7.5, 25 mM NaCl, 5 mM EDTA) containing 2 mM GTP or GTPγS, for 30 min at 30°C. Samples were chilled on ice and $MgCl_2$ was added to a final concentration of 10 mM. RGL3-RBD was used as a positive control for nucleotide loading due to the GTP-dependent interaction between RIT1 and RGL3.[55]

For GST pulldown of proteins from cell lysates, 3 x 10^6 HEK-293T cells were transfected with 4 μg total DNA of indicated plasmids. 24 hours after transfection, cells were rinsed with ice-cold PBS and lysed with 1 ml of Lysis buffer (50 mM Tris-HCl (pH 8.0), 150 mM NaCl, 1% IGEPAL CA-630, 10% glycerol) supplemented with protease and phosphatase inhibitor cocktails (Sigma-Aldrich). Lysates were cleared by centrifugation and incubated with 20 μl of Glutathione Sepharose 4B beads for 4 h at 4°C with end over end rotation. Beads were rinsed three times with Lysis buffer and resuspended in LDS sample buffer.

For immunoprecipitation of FLAG-RIT1 from cell cycle synchronized HeLa cells, approximately 10^6 cells were rinsed with PBS and harvested using a cell scraper at indicated time points, spun down and frozen. Cells were then lysed with RIPA Buffer (50 mM Tris-HCl (pH 8.0), 150 mM NaCl, 0.5% Deoxycholate, 0.1% SDS, 1% IGEPAL CA-630) supplemented with protease and phosphatase inhibitor cocktails (Sigma-Aldrich), cleared by centrifugation, and incubated with 20 μl anti-FLAG M2 agarose beads (EMD Millipore) for 4 hours at 4°C with end over end rotation. Beads were rinsed three times with RIPA buffer and resuspended in LDS sample buffer.

Cell cycle synchronization—Synchronization of cells at G1/S boundary was performed with a double thymidine block. Briefly, ~50% confluent cells were treated with 2 mM thymidine (Sigma-Aldrich) for 20 h, rinsed twice and released into drug-free media for 9 h, then treated again with 2 mM thymidine for 18 h. Synchronization of cells in prometaphase was done by addition of 100 ng/ml nocodazole (Selleckchem) 4 h after release from a single-thymidine block and incubated for 10 h. Mitotic cells were collected by mechanical shake off.

Subcellular protein fractionation—For subcellular fractionation of endogenous RIT1, Asynchronous cells were harvested with trypsin-EDTA and then centrifuged at 500 x *g* for 5 min. Nocodazole-arrested mitotic cells were harvested by mitotic shake-off and centrifuged at 500 x *g* for 5 min. Cell pellets were rinsed with ice-cold PBS and transferred to 1.5 ml tubes and pelleted by centrifugation at 500 x *g* for 5 min. Cell pellets were then lysed and proteins were fractionated using the Subcellular Protein Fractionation Kit for Cultured Cells (Thermo Scientific) according to manufacturer's instructions.

Liposome Binding Assay—Liposomes were prepared by mixing chloroform solutions of POPC and POPS (70:30) (Avanti Polar Lipids), desiccated under nitrogen gas, and stored in a vacuum overnight. Lipids were then redissolved in TBS (20 mM Tris HCl pH 7.5, 100mM NaCl, 0.02% sodium azide) to a final 1 mM phospholipid concentration and subjected to five freeze-thaw cycles. Lipid suspension was then filtered through a 0.1 μm

pore size membrane in a mini-extruder (Avanti Polar Lipids) ten times to generate uniform unilamellar vesicles. For liposome binding assay, 100 µl reactions containing 0.1 µM RIT1 with or without 0.1 µM MAD2 and/or p31^{comet} protein in TBS were incubated on ice for 1 h. Liposomes were then added to each reaction at a final lipid concentration of 100 µM and incubated on ice for an additional 1 h. Liposomes were pelleted by ultracentrifugation (100,000 x *g*) for 30 min. Pellets were dissolved in 1x LDS and analyzed by Western blot.

Size Exclusion Chromatography—Equal molar ratios of indicated proteins were incubated at 10 µM final concentration in PBS (pH 7.4), 0.5 mM TCEP for 1 hour at 25°C. Samples were chilled on ice and centrifuged (15,000 rpm) to remove any precipitates before loading onto a Superdex 200 3.2/300 column equilibrated in PBS (pH 7.4), 0.5 mM TCEP. All samples were eluted under isocratic conditions at 4°C with a flow rate of 0.035 ml min^{-1}. Elution profiles were monitored at 280nm. Elution fractions were separated by SDS-PAGE and stained with Coomassie. Consistent with previous reports, we observed spontaneous dimerization of bacterially expressed MAD2 (see figure S1D).[39,56]

Immunofluorescence and Metaphase spreads—For immunofluorescence microscopy, cells were grown of #1.5 coverslips, rinsed with PBS, and fixed with 4% paraformaldehyde in PBS for 10 min at room temperature. Permeabilization was performed with 0.1% Triton X-100 for 10 min at room temperature (RT) and blocked with blocking buffer (3% BSA in 0.1 % PBS-Tween 20) for 1 h or overnight at 4C. Primary and secondary antibodies were diluted in blocking buffer. Cells were incubated with primary antibody for 1 h at RT, rinsed 3x with PBS-T, then incubated with secondary antibody for 1 h at RT. Cells were counterstained with DAPI (Sigma Aldrich) and mounted with Fluoromount-G (Invitrogen). The following antibodies were used: FLAG (F1804; 1:1000) and Closed-MAD2 (Jakob Nilsson, University of Copenhagen; 1:50), Alexa Fluor 488, and Alexa Fluor 647 (Life Technologies, 1:2,000), CREST-FITC (Antibodies Inc.; 1:50). For subcellular localization of FLAG-RIT1, images were acquired on an inverted Nikon Ti microscope equipped with a CSU-22 spinning disk confocal, EMCCD camera. Images were processed in Fiji.[50] For MAD2 kinetochore intensity experiments, images were acquired on a GE OMX-SR microscope (inverted) equipped with three PCO 15bit CMOS cameras and a Plan ApoN 60X/1.42 oil objective. Deconvolved z-stack images were processed and quantified in Fiji. MAD2 mean fluorescence at kinetochores was normalized to CREST mean fluorescence signal.

For analysis of mitotic errors (chromosome segregation errors), HCT-116 cells were grown on #1.5 coverslips, rinsed with PBS, and fixed with 100% methanol. Coverslips were quickly hydrated and mounted with Prolong Gold Antifade mounting media with DAPI (Invitrogen). Cells were imaged on a Zeiss AxioImager M1 fluorescent microscope equipped with a 40x/0.75 Plan-Neofluar objective (Zeiss) and controlled with ZEN imaging software (Zeiss). For each biological replicate, at least 60 anaphase cells were analyzed per condition.

For metaphase chromosome spread analysis, cells were treated with 0.1 µg/ml Colcemid (Thermo Fisher Scientific) for 2 h, trypsinized and spun down. Cell pellets were gently resuspended in 2 ml hypotonic solution (75 mM KCl) added dropwise while mixing

cell suspension, followed by 15 min incubation at 37°C. Cells were spun down again and resuspended in 5 ml of Carnoy's fixative (3:1, methanol:glacial acetic acid, made fresh) added dropwise to cells. Cells were allowed to fix at room temperature for 20 min, then centrifuged and rinsed twice with Carnoy's fixative. Cells were dropped onto clean coverslips and rinsed with fixative to remove debris. Coverslips were placed in a humidity chamber for 10 min, then allowed to air dry for 24-72 h. Chromosome spreads were mounted with ProLong Gold Antifade mounting medium with DAPI (Thermo Fisher Scientific) and imaged on a Zeiss AxioImager M1 fluorescent microscope equipped with a 63x/1.25 Plan-Neofluar oil objective (Zeiss). Images of at least 75 chromosome spreads were captured per condition and experimenter blinded before being quantified using Fiji.[50]

Live cell imaging—For mitotic duration experiments, cells were engineered to stably express Histone H2B-mCherry (pLenti6-H2B-mCherry, Addgene, plasmid #89766), and seeded onto 12-well #1.5 glass bottom plates (Cellvis). Drug treatments were performed 1 h before imaging. Time-lapse images were captured on a Nikon Ti-E inverted wide-field fluorescent microscope equipped with a 20x/0.75 Plan Apo air objective (Nikon). Cells treated with nocodazole were imaged at 5 min intervals, otherwise cells were imaged at 2 min, for 20 hours. The microscope was equipped with an incubation chamber (Okolab), providing a humidified atmosphere at 37 °C with 5% CO2. Mitotic length was quantified as the duration between nuclear disassembly and anaphase onset. Mitotic error rates in hTERT-RPE1 cells were determined from live-cell images used to assess mitotic length. Images were analyzed using Fiji.

For RIT1 subcellular localization experiments, hTERT-RPE1 cells stably expressing Histone H2B-mCherry and mNeonGreen (mNG)-RIT1 were seeded on seeded onto 12-well #1.5 glass bottom plates and allowed to adhere for 24-48 h. Prior to imaging, cells were exchanged into imaging media: FluoroBrite DMEM (Thermo Fisher Scientific) supplemented with 10% FBS and 4 mM GlutaMAX (Thermo Fisher Scientific). Images were acquired as a series of 0.9 μm z-stacks with a Plan Apo 40x/0.95 Corr (DIC N2 / 40X I) 227.5 nm/pixel objective (Nikon) at 5 min intervals on a Nikon Ti-E inverted CSU-22 spinning disk confocal microscope equipped with an incubation chamber (Okolab), providing a humidified atmosphere at 37 °C with 5% CO2. Images were analyzed using Fiji. For quantitative analysis, a single central plane along the z-axis was used. For PM/Cyto. ratio calculations, semi-automated recognition of the cell boundary within the Fiji program was used to create regions of interests designating the plasma membrane and cytoplasm, and mean fluorescence intensity was calculated within each region.

For Cyclin B1 degradation assays, hTERT-RPE1 and HeLa cells stably expressing low levels of mNG-Cyclin B1 under the transcriptional control of a Ubiquitin C promoter and Histone H2B-mCherry were seeded onto chambered coverslips (Ibidi) and imaged similarly to the RIT1 subcellular localization experiments described above with the following exceptions: images of unperturbed mitosis were captured at 2 min intervals and images of cells treated with nocodazole at 6 min intervals. For quantitative analysis, a single central plane along the z-axis was used. mNG mean fluorescence intensity was normalized to NEBD.

Kinase Assays—For phosphorylation of RIT1 using mitotic cell extract, metaphase arrested HEK-293T cells were harvested, rinsed with PBS, and lysed with 4x pellet volume of Lysis buffer (50 mM Tris-HCl (pH 8.0), 150 mM NaCl, 1% IGEPAL CA-630, 10% glycerol) supplemented with 10 μM MG132 (Sigma-Aldrich) protease and phosphatase inhibitor cocktails (Sigma-Aldrich). The lysate was cleared by centrifugation for 10 min at 15,000 rpm. 1 ml of cleared lysate was incubated with indicated drugs (10 μM final concentration) or DMSO for 30 min at 4°C. No lysate control consisted of 1 ml Lysis buffer. Bacteria purified GST-RIT1 or GST protein bound to sepharose beads was added to lysates at 0.5 μM final concentration, together with 10 mM $MgCl_2$ and 0.1 mM ATP. Reactions were incubated at 30°C for 1 h with end over end rotation. Tubes were chilled on ice for 5 min, beads were then centrifuged and rinsed three times with RIPA buffer and resuspended in LDS sample buffer.

CDK1/Cyclin B1 kinase assays were conducted using recombinant active CDK1/Cyclin B1 purchased from SignalChem (C22-10G). 20 μl reactions containing 200 ng CDK1/Cyclin B1 protein and 3 μg of RIT1 protein diluted in Kinase assay buffer (5 mM MOPS, pH7.2, 2.5 mM β-glycerol-phosphate, 10 mM $MgCl_2$, 1 mM EGTA, 0.4 mM EDTA, 50 ng/μl BSA) with or without 3mM ATP were incubated at 30°C for 1 h. Reactions were stopped by addition of LDS sample buffer for SDS-PAGE or flash-frozen in liquid nitrogen for mass spectrometry analysis.

Mass Spectrometry—For identification of RIT1 binding partners, approximately 2 x 10^7 HEK-293T cells were transiently transfected with 8 μg of plasmid (FLAG-RIT1 or EV control) and immunoprecipitated as described above with buffer containing 50 mM Tris-HCl (pH 8.0), 150 mM NaCl, 1% IGEPAL CA-630, 10% glycerol and supplemented with protease and phosphatase inhibitor cocktails (Sigma-Aldrich). Magnetized beads were washed with ice-cold 20 mM Tris-HCl (pH 8.0), 2 mM $CaCl_2$ buffer and frozen prior to trypsin digest.

Protein pulldown samples were on-bead digested with trypsin as previously described.[11] Briefly, the beads were resuspended in 9 μL of 20 mM Tris-HCl pH 8.0. The proteins were reduced with DTT, 5 mM final concentration, at room temperature for 30 min; alkylated with iodoacetamide, 15 mM final concentration, at room temperature for 10 min; and digested with 500 ng of trypsin (Sigma Trypsin Singles, T7575) at 37°C overnight. In vitro kinase assay samples, 20 μL each, were digested using the same protocol. All samples were desalted with ZipTip u-C18 pipette tips (Millipore), vacuum dried, and reconstituted in 15 μL of 0.1% formic acid for analysis by LC-MS/MS.

LC-MS/MS was carried out on Acquity UPLC M-Class system (Waters) online with Orbitrap Fusion Lumos Tribrid Mass Spectrometer (Thermo Fisher Scientific). Reversed-phase chromatography was performed on a 15 cm silica-C18 EasySpray column (Thermo Fisher Scientific) at 45°C with a binary buffer system (Buffer A = 0.1% formic acid in water; Buffer B = 0.1% formic acid in acetonitrile) and a flow rate of 400 nL/min. The sample was loaded at 2% B for 20 min followed by a 2-60% B gradient over 60 min, followed by a brief wash at 80% B and equilibration at 2% B. The mass spectrometer was operated in Full-MS/ddMS2 mode with one survey scan (375-1500 m/z, R=120,000, AGC

target of 4e5), followed by a series of data-dependent HCD MS2 scans not to exceed a 3 sec cycle (AGC target of 5e4, max IT 100 ms, R=30,000, isolation window 1.6 m/z, NCE 30%, stepped collision 5%, and 30 s dynamic exclusion).

MS raw data files were converted to peak list files using Proteome Discoverer v. 1.4 (Thermo Fisher Scientific) and searched using Protein Prospector[57,58] (version 6.0.0) against human SwissProt database[59] downloaded on 01/08/2018 (or a subset of this database with RIT1, CDK1 and CCNB1 entries only when searching in vitro kinase assay samples) and a corresponding random concatenated decoy database. Other settings included the default "ESI-Q-high-res" parameters with trypsin as the protease, up to two allowed missed cleavage sites, Carbamidomethyl-C as a constant modification, default variable modifications for pulldown samples (or default variable modifications plus phosphorylation at STY for in vitro kinase assay samples), up to 3 modifications per peptide, and 5 ppm precursor mass and 15 ppm fragment mass tolerance. False discovery rate of <1% was used as the cutoff for peptide expectation values. Protein Prospector search results were exported in BiblioSpec format compatible with downstream analysis in Skyline.[51] Quantitation of peptide and protein abundances was carried out in Skyline v20 by quantifying MS1 precursor peak areas with normalization by median centering.[60] Peptides shared by multiple proteins in the database were excluded.

APC/C Ubiquitination Assay—Detection of APC/C activity using mitotic checkpoint active cell extracts was previously described.[61] HeLa RIT1 KO cells arrested in prometaphase were harvested, rinsed with ice-cold PBS, and resuspended in 75% pellet volume of hypotonic buffer (20 mM HEPES, pH 7.6, 5 mM KCl, 1 mM DTT) containing protease inhibitor cocktail (Roche). Cells were lysed with multiple rounds of freeze-thawing and were cleared by centrifugation at 13,000 rpm for 1 h at 4°C. Cleared lysate was supplemented with glycerol to 10% (v/v), aliquoted and frozen in liquid nitrogen. The protein concentration of cell extract was ~20 mg/ml. APC/C activity reactions were carried in samples containing 50% (v/v) mitotic cell extract diluted in buffer with final concentrations of the following: 10 mM Tris-HCl, pH 7.6, 5 mM $MgCl_2$, 1 mM DTT, 1 mg/ml Ubiquitin (Boston Biochem; U-100H), 10 mM phosphocreatine, 0.5 mM ATP, 10 μg/ml UbcH10 (Boston Biochem; E2-650), and 50 μg/ml Creatine phosphokinase (Sigma-Aldrich). Recombinant RIT1 protein was buffer exchanged into assay buffer containing 20 mM HEPES pH 7.4, 300 mM NaCl, 1 mM TCEP, 5% glycerol before being added to samples. Control conditions received equal volumes of assay buffer. Samples were incubated on ice for 1 h, then transferred to 30°C. 4 μl samples were withdrawn at indicated times and rapidly quenched with LDS sample buffer. Degradation of Cyclin B1 and Securin was followed by immunoblotting and was normalized to MAD2 protein levels. Densitometry analysis was performed using Fiji.

QUANTIFICATION AND STATISTICAL ANALYSIS

Statistical analysis was performed using GraphPad Prism 7.0 (GraphPad). Results are expressed as mean ± s.d. For each mitotic length scatterplot, the horizontal line represents the mean. For kinetochore MAD2 fluorescence intensity scatterplots, the horizontal line and error bars represents the median and 95% confidence interval, respectively. No

statistical methods were used to predetermine the sample size. Experiments analyzed by immunoblotting were repeated 2-4 times with similar results. For chromosome spread analysis, investigators were blinded to sample allocation.

Supplementary Material

Refer to Web version on PubMed Central for supplementary material.

ACKNOWLEDGEMENTS

We thank Dom Esposito and Vanessa Wall (Frederick National Lab) for the multisite gateway plasmid toolkit and members of the McCormick lab for their input. We thank Alice Berger and Athea Vichas (Fred Hutch Cancer Center) for kindly sharing unpublished data and Jakob Nilsson (University of Copenhagen) for C-MAD2 antibody. Data for this study were acquired at the Nikon Imaging Center at UCSF. This work was supported by a grant from the NCI (R35CA197709 to F.M.). ACN is a fellow of the NSF Graduate Research Fellowship Program (1650113). P.C. work is supported by the NCI (K99CA245122). We thank the UCSF Mass Spectrometry Facility and A. L. Burlingame for providing MS instrumentation support for this project (funded by the NIH grants P41GM103481 and S10OD016229).

REFERENCES

1. Musacchio A (2015). The Molecular Biology of Spindle Assembly Checkpoint Signaling Dynamics. Curr. Biol 25, R1002–1018. [PubMed: 26485365]
2. Musacchio A, and Salmon ED (2007). The spindle-assembly checkpoint in space and time. Nat. Rev. Mol. Cell Biol 8, 379–393. [PubMed: 17426725]
3. Ben-David U, and Amon A (2020). Context is everything: aneuploidy in cancer. Nat. Rev. Genet 21, 44–62. [PubMed: 31548659]
4. Oromendia AB, and Amon A (2014). Aneuploidy: implications for protein homeostasis and disease. Dis Model Mech 7, 15–20. [PubMed: 24396150]
5. Simanshu DK, Nissley DV, and McCormick F (2017). RAS Proteins and Their Regulators in Human Disease. Cell 170, 17–33. [PubMed: 28666118]
6. Van R, Cuevas-Navarro A, Castel P, and McCormick F (2020). The molecular functions of RIT1 and its contribution to human disease. Biochemical Journal 477, 2755–2770.
7. Berger AH, Imielinski M, Duke F, Wala J, Kaplan N, Shi G-X, Andres DA, and Meyerson M (2014). Oncogenic RIT1 mutations in lung adenocarcinoma. Oncogene 33, 4418–4423. [PubMed: 24469055]
8. Aoki Y, Niihori T, Banjo T, Okamoto N, Mizuno S, Kurosawa K, Ogata T, Takada F, Yano M, Ando T, et al. (2013). Gain-of-function mutations in RIT1 cause Noonan syndrome, a RAS/MAPK pathway syndrome. Am. J. Hum. Genet 93, 173–180. [PubMed: 23791108]
9. Yaoita M, Niihori T, Mizuno S, Okamoto N, Hayashi S, Watanabe A, Yokozawa M, Suzumura H, Nakahara A, Nakano Y, et al. (2016). Spectrum of mutations and genotype-phenotype analysis in Noonan syndrome patients with RIT1 mutations. Hum. Genet 135, 209–222. [PubMed: 26714497]
10. Rodriguez-Viciana P, Sabatier C, and McCormick F (2004). Signaling specificity by Ras family GTPases is determined by the full spectrum of effectors they regulate. Mol. Cell. Biol 24, 4943–4954. [PubMed: 15143186]
11. Castel P, Cheng A, Cuevas-Navarro A, Everman DB, Papageorge AG, Simanshu DK, Tankka A, Galeas J, Urisman A, and McCormick F (2019). RIT1 oncoproteins escape LZTR1-mediated proteolysis. Science 363, 1226–1230. [PubMed: 30872527]
12. Hagan RS, Manak MS, Buch HK, Meier MG, Meraldi P, Shah JV, and Sorger PK (2011). p31(comet) acts to ensure timely spindle checkpoint silencing subsequent to kinetochore attachment. Mol. Biol. Cell 22, 4236–4246. [PubMed: 21965286]
13. Xia G, Luo X, Habu T, Rizo J, Matsumoto T, and Yu H (2004). Conformation-specific binding of p31(comet) antagonizes the function of Mad2 in the spindle checkpoint. EMBO J. 23, 3133–3143. [PubMed: 15257285]

14. Wang L, Zhang J, Wan L, Zhou X, Wang Z, and Wei W (2015). Targeting Cdc20 as a novel cancer therapeutic strategy. Pharmacol Ther 151, 141–151. [PubMed: 25850036]
15. Westhorpe FG, Tighe A, Lara-Gonzalez P, and Taylor SS (2011). p31comet-mediated extraction of Mad2 from the MCC promotes efficient mitotic exit. J. Cell. Sci 124, 3905–3916. [PubMed: 22100920]
16. Eytan E, Wang K, Miniowitz-Shemtov S, Sitry-Shevah D, Kaisari S, Yen TJ, Liu S-T, and Hershko A (2014). Disassembly of mitotic checkpoint complexes by the joint action of the AAA-ATPase TRIP13 and p31comet. Proceedings of the National Academy of Sciences 111, 12019–12024.
17. Habu T, Kim SH, Weinstein J, and Matsumoto T (2002). Identification of a MAD2-binding protein, CMT2, and its role in mitosis. EMBO J. 21, 6419–6428. [PubMed: 12456649]
18. Mapelli M, Massimiliano L, Santaguida S, and Musacchio A (2007). The Mad2 conformational dimer: structure and implications for the spindle assembly checkpoint. Cell 131, 730–743. [PubMed: 18022367]
19. Yang M, Li B, Tomchick DR, Machius M, Rizo J, Yu H, and Luo X (2007). p31comet blocks Mad2 activation through structural mimicry. Cell 131, 744–755. [PubMed: 18022368]
20. Mapelli M, Filipp FV, Rancati G, Massimiliano L, Nezi L, Stier G, Hagan RS, Confalonieri S, Piatti S, Sattler M, et al. (2006). Determinants of conformational dimerization of Mad2 and its inhibition by p31comet. EMBO J. 25, 1273–1284. [PubMed: 16525508]
21. Lee CH, Della NG, Chew CE, and Zack DJ (1996). Rin, a neuron-specific and calmodulin-binding small G-protein, and Rit define a novel subfamily of ras proteins. J. Neurosci 16, 6784–6794. [PubMed: 8824319]
22. Heo WD, Inoue T, Park WS, Kim ML, Park BO, Wandless TJ, and Meyer T (2006). PI(3,4,5)P3 and PI(4,5)P2 lipids target proteins with polybasic clusters to the plasma membrane. Science 314, 1458–1461. [PubMed: 17095657]
23. Hall FL, and Vulliet PR (1991). Proline-directed protein phosphorylation and cell cycle regulation. Curr. Opin. Cell Biol 3, 176–184. [PubMed: 1831990]
24. Lindqvist A, Rodríguez-Bravo V, and Medema RH (2009). The decision to enter mitosis: feedback and redundancy in the mitotic entry network. J. Cell Biol 185, 193–202. [PubMed: 19364923]
25. Santaguida S, Tighe A, D'Alise AM, Taylor SS, and Musacchio A (2010). Dissecting the role of MPS1 in chromosome biorientation and the spindle checkpoint through the small molecule inhibitor reversine. J. Cell Biol 190, 73–87. [PubMed: 20624901]
26. Dobles M, Liberal V, Scott ML, Benezra R, and Sorger PK (2000). Chromosome missegregation and apoptosis in mice lacking the mitotic checkpoint protein Mad2. Cell 101, 635–645. [PubMed: 10892650]
27. Hanks S, Coleman K, Reid S, Plaja A, Firth H, Fitzpatrick D, Kidd A, Méhes K, Nash R, Robin N, et al. (2004). Constitutional aneuploidy and cancer predisposition caused by biallelic mutations in BUB1B. Nat. Genet 36, 1159–1161. [PubMed: 15475955]
28. Iwanaga Y, Chi Y-H, Miyazato A, Sheleg S, Haller K, Peloponese J-M, Li Y, Ward JM, Benezra R, and Jeang K-T (2007). Heterozygous deletion of mitotic arrest-deficient protein 1 (MAD1) increases the incidence of tumors in mice. Cancer Res. 67, 160–166. [PubMed: 17210695]
29. Li M, Fang X, Wei Z, York JP, and Zhang P (2009). Loss of spindle assembly checkpoint-mediated inhibition of Cdc20 promotes tumorigenesis in mice. J. Cell Biol 185, 983–994. [PubMed: 19528295]
30. Michel LS, Liberal V, Chatterjee A, Kirchwegger R, Pasche B, Gerald W, Dobles M, Sorger PK, Murty VV, and Benezra R (2001). MAD2 haplo-insufficiency causes premature anaphase and chromosome instability in mammalian cells. Nature 409, 355–359. [PubMed: 11201745]
31. Lengauer C, Kinzler KW, and Vogelstein B (1997). Genetic instability in colorectal cancers. Nature 386, 623–627. [PubMed: 9121588]
32. DeAntoni A, Sala V, and Musacchio A (2005). Explaining the oligomerization properties of the spindle assembly checkpoint protein Mad2. Philos. Trans. R. Soc. Lond., B, Biol. Sci 360, 637–647, discussion 447-448. [PubMed: 15897186]
33. Sironi L, Mapelli M, Knapp S, De Antoni A, Jeang K-T, and Musacchio A (2002). Crystal structure of the tetrameric Mad1-Mad2 core complex: implications of a "safety belt" binding mechanism for the spindle checkpoint. EMBO J. 21, 2496–2506. [PubMed: 12006501]

34. Hara M, Özkan E, Sun H, Yu H, and Luo X (2015). Structure of an intermediate conformer of the spindle checkpoint protein Mad2. Proc. Natl. Acad. Sci. U.S.A 112, 11252–11257. [PubMed: 26305957]
35. Luo X, Tang Z, Rizo J, and Yu H (2002). The Mad2 spindle checkpoint protein undergoes similar major conformational changes upon binding to either Mad1 or Cdc20. Mol. Cell 9, 59–71. [PubMed: 11804586]
36. Mondal G, Baral RN, and Roychoudhury S (2006). A new Mad2-interacting domain of Cdc20 is critical for the function of Mad2-Cdc20 complex in the spindle assembly checkpoint. Biochem. J 396, 243–253. [PubMed: 16497171]
37. Kim S, Sun H, Ball HL, Wassmann K, Luo X, and Yu H (2010). Phosphorylation of the spindle checkpoint protein Mad2 regulates its conformational transition. Proc. Natl. Acad. Sci. U.S.A 107, 19772–19777. [PubMed: 21041666]
38. Luo X, Fang G, Coldiron M, Lin Y, Yu H, Kirschner MW, and Wagner G (2000). Structure of the Mad2 spindle assembly checkpoint protein and its interaction with Cdc20. Nat. Struct. Biol 7, 224–229. [PubMed: 10700282]
39. Sironi L, Melixetian M, Faretta M, Prosperini E, Helin K, and Musacchio A (2001). Mad2 binding to Mad1 and Cdc20, rather than oligomerization, is required for the spindle checkpoint. EMBO J. 20, 6371–6382. [PubMed: 11707408]
40. Wang K, Sturt-Gillespie B, Hittle JC, Macdonald D, Chan GK, Yen TJ, and Liu S-T (2014). Thyroid Hormone Receptor Interacting Protein 13 (TRIP13) AAA-ATPase Is a Novel Mitotic Checkpoint-silencing Protein. J. Biol. Chem 289, 23928–23937. [PubMed: 25012665]
41. Primorac I, and Musacchio A (2013). Panta rhei: the APC/C at steady state. J. Cell Biol 201, 177–189. [PubMed: 23589490]
42. Chang L, and Barford D (2014). Insights into the anaphase-promoting complex: a molecular machine that regulates mitosis. Curr. Opin. Struct. Biol 29, 1–9. [PubMed: 25174288]
43. Hochegger H, Takeda S, and Hunt T (2008). Cyclin-dependent kinases and cell-cycle transitions: does one fit all? Nat Rev Mol Cell Biol 9, 910–916. [PubMed: 18813291]
44. Hingorani SR, Wang L, Multani AS, Combs C, Deramaudt TB, Hruban RH, Rustgi AK, Chang S, and Tuveson DA (2005). Trp53R172H and KrasG12D cooperate to promote chromosomal instability and widely metastatic pancreatic ductal adenocarcinoma in mice. Cancer Cell 7, 469–483. [PubMed: 15894267]
45. Kamata T, and Pritchard C (2011). Mechanisms of aneuploidy induction by RAS and RAF oncogenes. Am J Cancer Res 1, 955–971. [PubMed: 22016838]
46. Yang G, Mercado-Uribe I, Multani AS, Sen S, Shih I-M, Wong K-K, Gershenson DM, and Liu J (2013). RAS promotes tumorigenesis through genomic instability induced by imbalanced expression of Aurora-A and BRCA2 in midbody during cytokinesis. Int. J. Cancer 133, 275–285. [PubMed: 23319376]
47. Sedgwick GG, Larsen MSY, Lischetti T, Streicher W, Jersie-Christensen RR, Olsen JV, and Nilsson J (2016). Conformation-specific anti-Mad2 monoclonal antibodies for the dissection of checkpoint signaling. MAbs 8, 689–697. [PubMed: 26986935]
48. Pemble H, Kumar P, van Haren J, and Wittmann T (2017). GSK3-mediated CLASP2 phosphorylation modulates kinetochore dynamics. J Cell Sci 130, 1404–1412. [PubMed: 28232523]
49. Ran FA, Hsu PD, Wright J, Agarwala V, Scott DA, and Zhang F (2013). Genome engineering using the CRISPR-Cas9 system. Nat Protoc 8, 2281–2308. [PubMed: 24157548]
50. Schindelin J, Arganda-Carreras I, Frise E, Kaynig V, Longair M, Pietzsch T, Preibisch S, Rueden C, Saalfeld S, Schmid B, et al. (2012). Fiji: an open-source platform for biological-image analysis. Nat. Methods 9, 676–682. [PubMed: 22743772]
51. Pino LK, Searle BC, Bollinger JG, Nunn B, MacLean B, and MacCoss MJ (2020). The Skyline ecosystem: Informatics for quantitative mass spectrometry proteomics. Mass Spectrom Rev 39, 229–244. [PubMed: 28691345]
52. Farnsworth CL, and Feig LA (1991). Dominant inhibitory mutations in the Mg(2+)-binding site of RasH prevent its activation by GTP. Mol. Cell. Biol 11, 4822. [PubMed: 1922022]

53. Frech M, Darden TA, Pedersen LG, Foley CK, Charifson PS, Anderson MW, and Wittinghofer A (1994). Role of glutamine-61 in the hydrolysis of GTP by p21H-ras: an experimental and theoretical study. Biochemistry 33, 3237–3244. [PubMed: 8136358]

54. Wall VE, Garvey LA, Mehalko JL, Procter LV, and Esposito D (2014). Combinatorial assembly of clone libraries using site-specific recombination. Methods Mol. Biol 1116, 193–208. [PubMed: 24395366]

55. Shao H, and Andres DA (2000). A novel RalGEF-like protein, RGL3, as a candidate effector for rit and Ras. J. Biol. Chem 275, 26914–26924. [PubMed: 10869344]

56. Fang G, Yu H, and Kirschner MW (1998). The checkpoint protein MAD2 and the mitotic regulator CDC20 form a ternary complex with the anaphase-promoting complex to control anaphase initiation. Genes Dev. 12, 1871–1883. [PubMed: 9637688]

57. Baker PR, Trinidad JC, and Chalkley RJ (2011). Modification site localization scoring integrated into a search engine. Mol. Cell Proteomics 10, M111.008078.

58. Chalkley RJ, and Baker PR (2017). Use of a glycosylation site database to improve glycopeptide identification from complex mixtures. Anal Bioanal Chem 409, 571–577. [PubMed: 27722944]

59. Consortium UniProt (2019). UniProt: a worldwide hub of protein knowledge. Nucleic Acids Res. 47, D506–D515. [PubMed: 30395287]

60. Schilling B, Rardin MJ, MacLean BX, Zawadzka AM, Frewen BE, Cusack MP, Sorensen DJ, Bereman MS, Jing E, Wu CC, et al. (2012). Platform-independent and label-free quantitation of proteomic data using MS1 extracted ion chromatograms in skyline: application to protein acetylation and phosphorylation. Mol. Cell Proteomics 11, 202–214. [PubMed: 22454539]

61. Braunstein I, Miniowitz S, Moshe Y, and Hershko A (2007). Inhibitory factors associated with anaphase-promoting complex/cylosome in mitotic checkpoint. Proc. Natl. Acad. Sci. U.S.A 104, 4870–4875. [PubMed: 17360335]

Highlights

- RIT1 directly interacts with SAC core components MAD2 and p31^{comet}
- CDK1 phosphorylates RIT1 during mitosis and inhibits its interaction with the SAC
- RIT1 is essential for timely progression through mitosis
- Pathogenic levels of RIT1 promote chromosome segregation errors

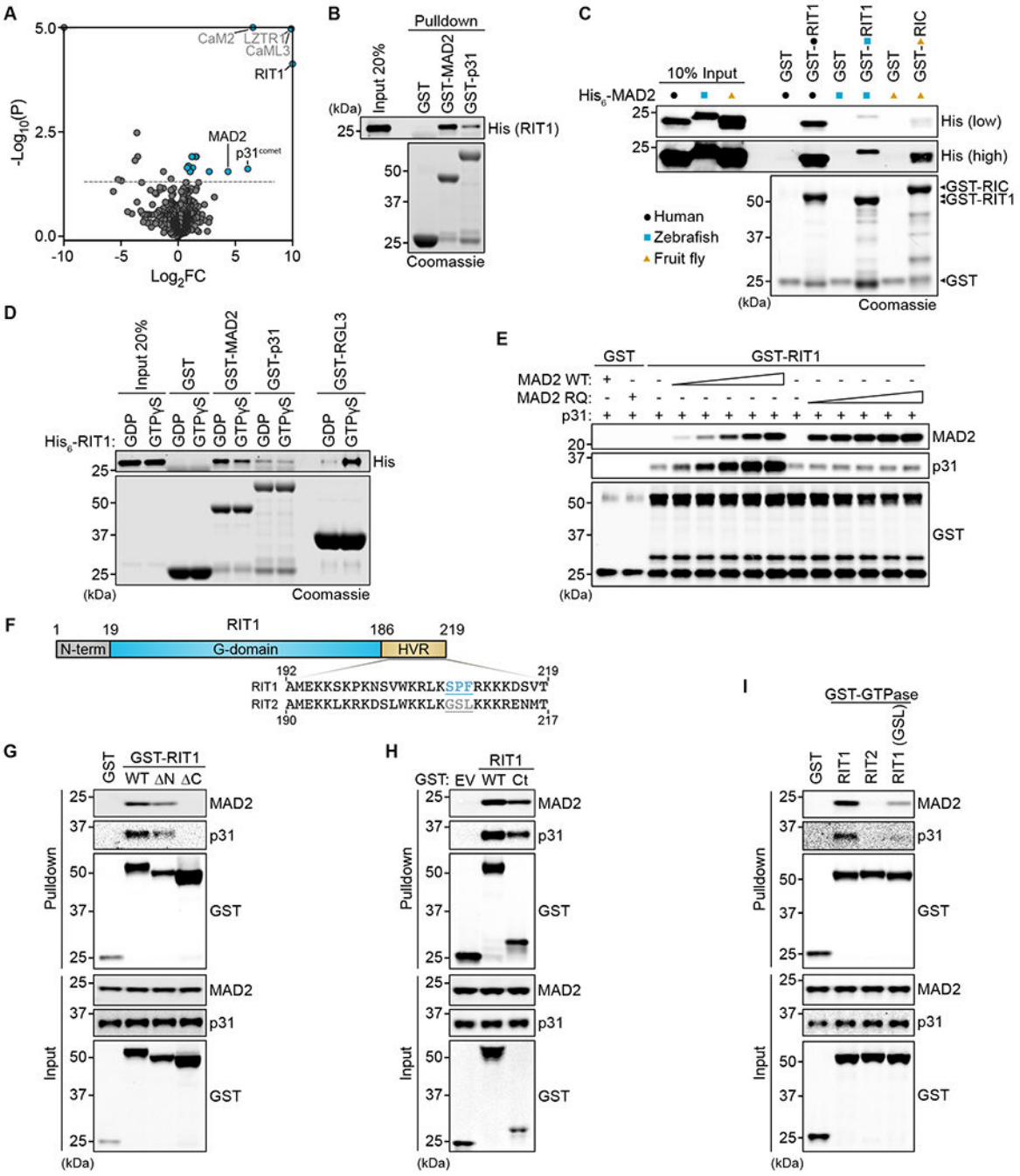

Figure 1. RIT1 interacts directly with the SAC proteins MAD2 and p31^{comet}

(**A**) Proteins obtained from lysates of HEK-293T cells transfected with FLAG-RIT1 or FLAG empty vector control were immunoprecipitated and analyzed by LC-MS/MS. Volcano plot shows enrichment of proteins detected in FLAG-RIT1 precipitates across three biologically independent repeats. Top hits included previously identified interactors: LZTR1, Calmodulin 2 (CaM2) and Calmodulin-like protein 3 (CaML3). Log_2 fold change (Log_2FC) and $-Log_{10}$ adjusted p-value ($-Log_{10}(P)$) were capped at 10 and 5.0, respectively. Dashed line represents p-value of 0.05.

(**B**) GST pulldown assay with indicated recombinant purified GST-tagged proteins and His_6-RIT1.
(**C**) GST pulldown assay with 0.1 μM of the indicated recombinant purified GST-tagged RIT1 (either human or zebrafish ortholog) or RIC (Fruit fly RIT1 ortholog) proteins and 0.1 μM of the different MAD2 orthologs.
(**D**) GST pulldown assay as in (B), with His_6-RIT1 protein loaded with GDP or GTPγS. GST-RGL3 serves as a positive control for nucleotide loading due to the GTP-dependent nature of the RIT1-RGL3 interaction.
(**E**) GST pulldown assay with 0.1 μM recombinant GST or GST-RIT1 incubated with 0.5 μM $p31^{comet}$ and titration of MAD2 WT or the dimerization and $p31^{comet}$ binding deficient mutant MAD2 R133E/Q134A (RQ) (0, 0.1, 0.2, 0.4, 0.8 or 1.6 μM).
(**F**) Schematic of RIT1 domain structure with amino acid sequence alignment of RIT1 and RIT2 C-terminal tails.
(**G**, **H, I**) Proteins pulled down from extracts of HEK-293T cells transfected with GST, GST-RIT1, or GST-RIT1 mutant constructs. Immunoblots were probed for endogenous MAD2 and $p31^{comet}$. EV, empty vector. Ct, C-terminal (192-219).
(**I**) RIT1 (GSL), RIT1 construct with residues 209-211 (SPF) replaced with corresponding RIT2 residues 207-209 (GSL).
See also Figure S1.

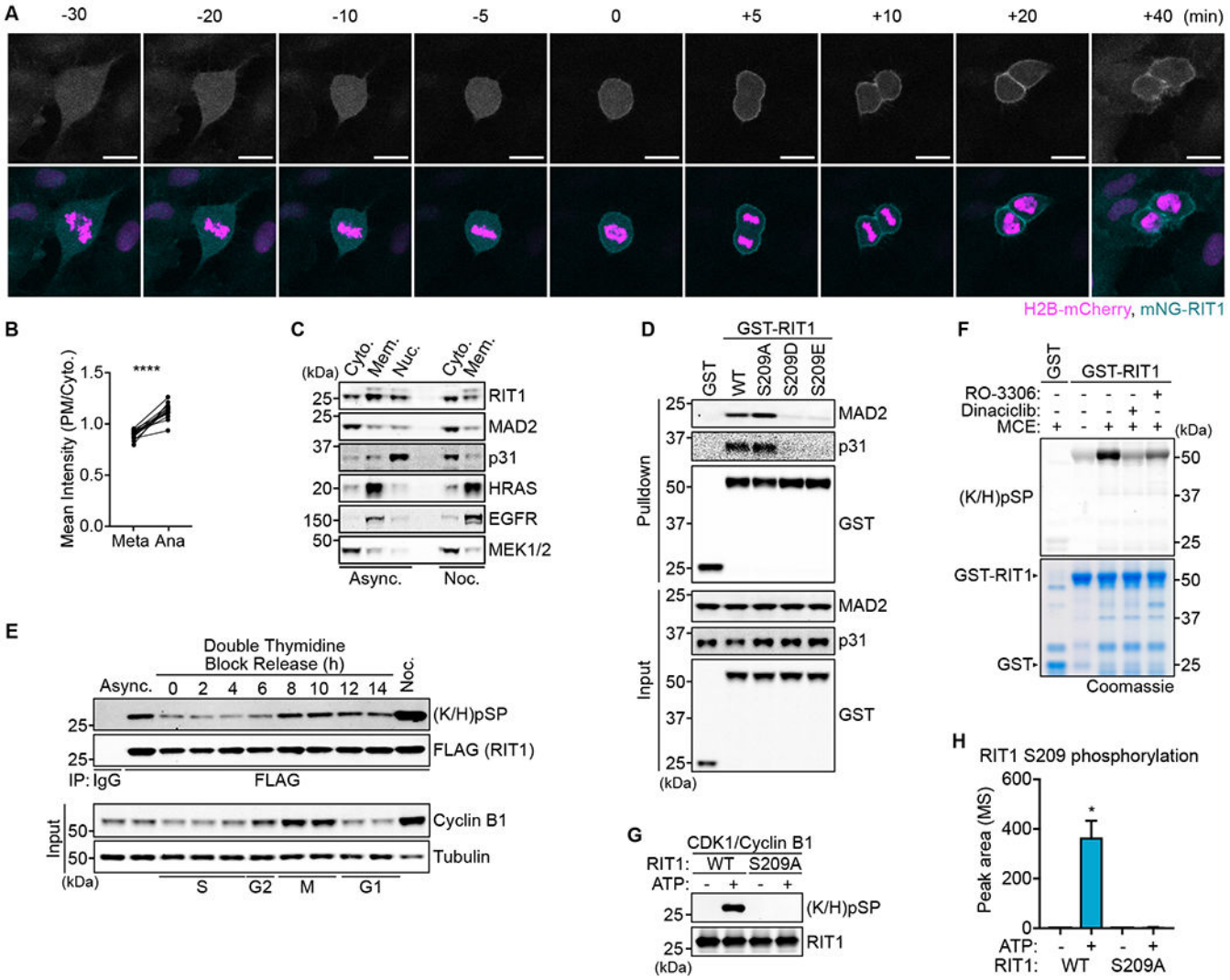

Figure 2. RIT1 interaction with MAD2 and p31^{comet} is regulated by CDK1 phosphorylation

(**A**) hTERT-RPE1 cell stably expressing mNeonGreen (mNG)-RIT1 and Histone H2B-mCherry undergoing mitosis imaged at 5 min intervals. Anaphase onset set to t = 0 min. Scale bar = 20 μm.

(**B**) Quantification of plasma membrane (PM) to cytoplasmic (Cyto.) ratio of mNG-RIT1 during metaphase (Meta, −5 min) and anaphase (Ana, +5 min) in cells as in (A). Two-sided Student's paired *t*-test, n = 15, ****$P \leq 0.0001$).

(**C**) Immunoblots of subcellular protein fractionation of HeLa cell lysates. Async., asynchronous growing cells. Noc., cells released from G1/S arrest for 4 hours then treated with 100 ng/ml nocodazole for 10 hours. HRAS included as a PM-bound protein control.

(**D**) Protein pulled down from extracts of HEK-293T cells transfected with GST or GST-RIT1 constructs. Immunoblots were probed for endogenous MAD2 and p31^{comet}.

(**E**) HeLa cells stably expressing FLAG-RIT1 released from a G1/S phase arrest and lysed at indicated time points. Immunoprecipitated proteins were probed for RIT1 S209 phosphorylation by immunoblotting. Async., asynchronous growing cells. Noc., cells released from G1/S arrest for 4 hours then treated with 100 ng/ml nocodazole for 10 hours.

(**F**) Detection of RIT1 S209 phosphorylation on bacterially expressed GST-RIT1 protein incubated with mitotic cell extract (MCE) treated with 1 μM Dinaciclib, 10 μM RO-3306, or DMSO control.

(**G**) Immunoblot of RIT1 S209 phosphorylation on bacterially expressed RIT1 proteins subjected to an *in vitro* kinase assay with recombinant active CDK1/Cyclin B1.

(**H**) MS quantification of phospho-S209 peptides in RIT1 protein incubated with CDK1/Cyclin B1 as in (G). ($n = 2$), Two-sided Student's *t*-test, data shown as mean, error bars indicate s.d., $*P \leq 0.05$.

See also Figure S2.

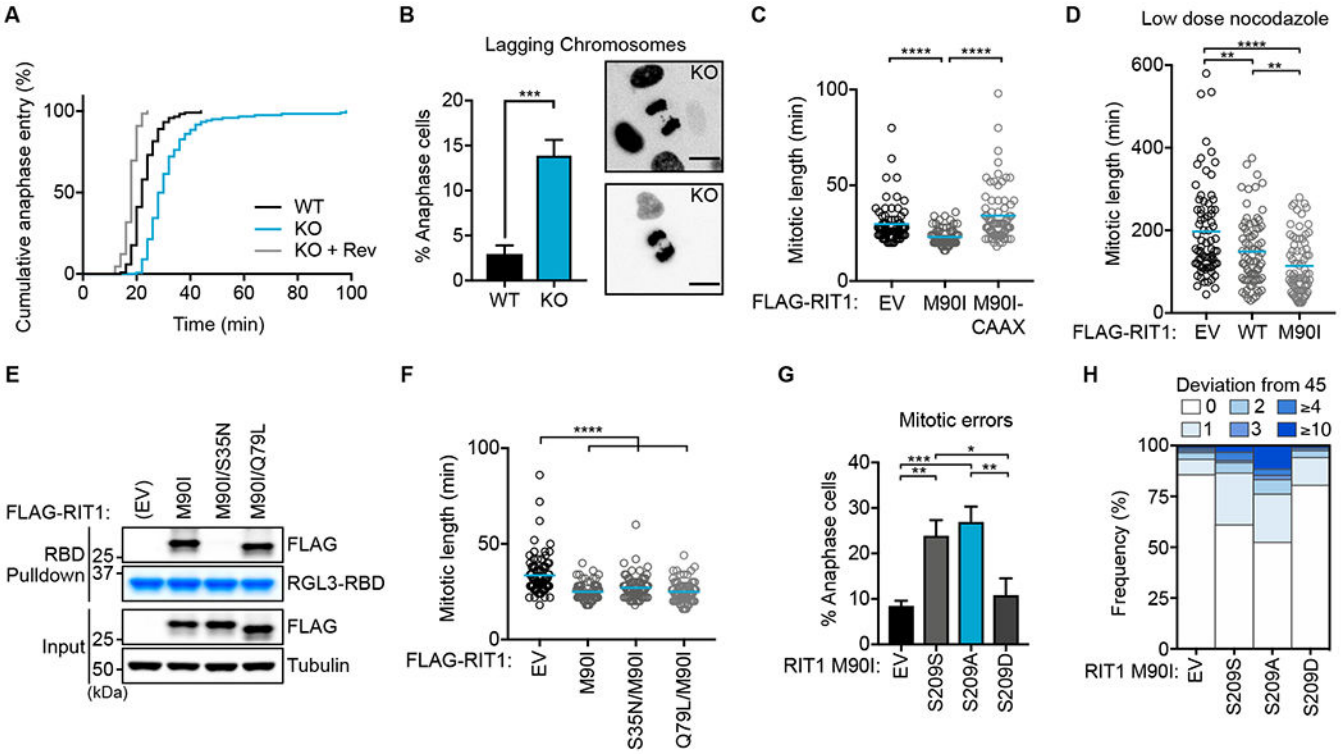

Figure 3. RIT1 regulates timely anaphase entry and chromosome segregation fidelity

(**A**) Comparison of mitotic transit times between WT and RIT1 KO hTERT-RPE1 cells assessed by time-lapse microscopy. Time measured from nuclear envelope breakdown (NEBD). Rev, cells treated with 1 μM Reversine. WT (n =119), KO (n = 122), KO + Rev (n = 66).

(**B**) Quantification of lagging chromosomes in anaphase hTERT RPE1 cells. Data represent three independent replicates with three WT clones and three KO clones. Error bars indicate s.d., ***$P \leq 0.001$.

(**C**, **D**) Duration of mitotic length (NEBD - anaphase onset) assessed by time-lapse microscopy in U2-OS cells stably expressing indicated proteins in (C) normal growth conditions [EV (n = 76), M90I (n = 66), M90I-CAAX (n = 72)] or (D) treated with 15 ng/ml nocodazole (n = 75). Two-sided Student's t-test, error bars indicate s.d., **$P \leq 0.01$, ***$P \leq 0.001$, ****$P \leq 0.0001$.

(**E**) Immunoblots of GST-RGL3 RBD pulldown assay with lysates from U2OS cells stably expressing indicated RIT1 constructs. RGL3-RBD protein stained with Coomassie.

(**F**) Duration of mitotic length (NEBD - anaphase onset) assessed by time-lapse microscopy in U2-OS cells stably expressing indicated proteins in normal growth conditions, EV (n = 81), M90I (n = 68), M90I/S35N (n = 75), M90I/Q79L (n = 77). Two-sided Student's t-test, error bars indicate s.d., ****$P \leq 0.0001$.

(**G**) Comparison of chromosome segregation error rates (lagging and bridging chromosomes) in HCT-116 cells stably expressing indicated constructs. EV, empty vector. Data represent three biologically independent repeats. Two-sided Student's t-test, error bars indicate s.d., *$P \leq 0.05$, **$P \leq 0.01$, ***$P \leq 0.001$.

(**H**) Metaphase spread assay compares frequency of aneuploidy, determined by a chromosome count other than the modal number, 45, in HCT-116 cells stably expressing EV ($n = 92$), S209S ($n = 98$), S209A ($n = 97$), or S209D ($n = 88$).
For (A, C, D, F-H), n indicates the number of cells or metaphase spreads counted and data shown is representative of at least two biologically independent experiments.
See also Figure S3.

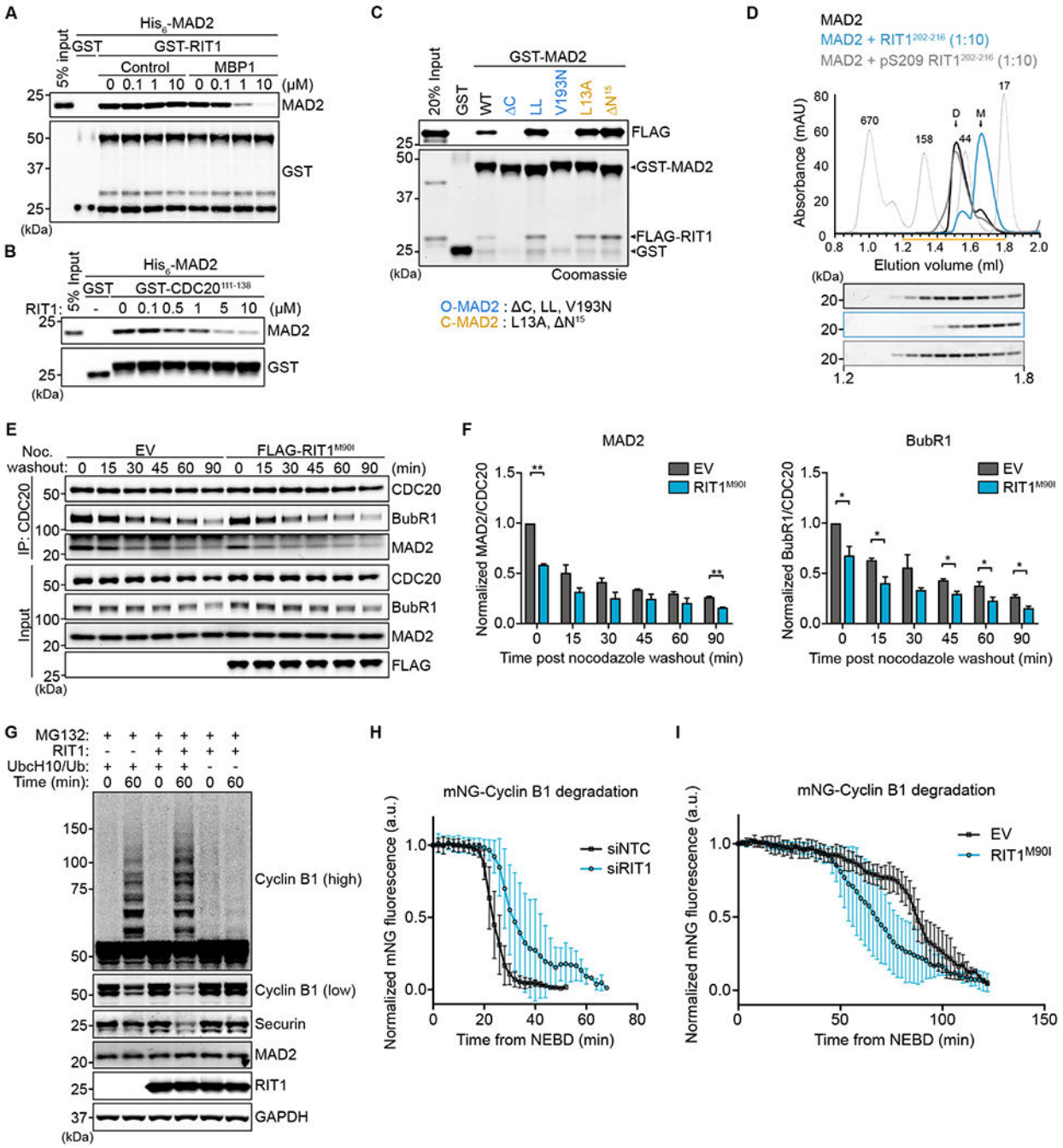

Figure 4. RIT1 inhibits MCC-MAD2 association and promotes degradation of APC/C substrates

(**A**, **B**) Immunoblots of precipitated proteins from an equilibrium competition pulldown assays with 0.2 μM recombinant (A) GST-RIT1 or (B) GST-CDC20 111-138 protein incubated with 0.2 μM His_6-MAD2 and titrating amounts of (A) MAD2 binding peptide 1 (MBP1) or a control peptide or (B) full-length RIT1 protein.

(**C**) Pulldown assay with 0.5 μM recombinant GST or GST-MAD2 proteins incubated with 0.5 μM FLAG-RIT1 protein. Precipitated proteins were separated by SDS-PAGE for immunoblot or Coomassie staining.

(**D**) Elution profile of MAD2 protein incubated with or without indicated peptides at 1:10 molar ratio for 1 hour at 25°C prior to gel filtration. The contents of 12 consecutive 50 μl fractions eluting between 1.2 ml to 1.8 ml are shown.
(**E**) Immunoblots of anti-CDC20 immunoprecipitated (IP) proteins from cells expressing empty vector (EV) or $RIT1^{M90I}$ at indicated time points following nocodazole washout. IP proteins probed from the same membrane.
(**F**) Quantification of data in (E); CoIP MAD2 or BubR1 band intensity normalized to CDC20 band intensity. Ratios normalized to EV time = 0 min. Two-sided Student's *t*-test, error bars indicate s.d., ($n = 2$) $*P \leq 0.05$, $**P \leq 0.01$.
(**G**) Immunoblots of samples from APC/C ubiquitination assay with and without 10 μM RIT1. To prevent degradation of ubiquitinated proteins, mitotic cell extracts were incubated with 10 μM MG132 for 1 hour on ice, prior to supplementation with additional ubiquitination assay components.
(H, I) Quantification of mNeon-Green (mNG)-Cyclin B1 mean intensity normalized to signal intensity at NEBD (t = 0), in H2B-mCherry expressing (H) RPE1 cells treated with indicated siRNA for 72 h prior to imaging ($n = 6$, from two independent experiments) or (I) HeLa cells expressing indicated constructs. Cells were imaged at 2 min intervals. ($n = 5$, from 2 independent experiments). Data represent mean ± s.d.
See also Figure S4.

KEY RESOURCES TABLE

REAGENT or RESOURCE	SOURCE	IDENTIFIER
Antibodies		
Phospho-p44/42 MAPK (Erk1/2) (Thr202/Tyr204) (D13.14.4E) XP Rabbit mAb	Cell Signaling Technology	Cat.# 4370
p44/42 MAPK (Erk1/2) (L34F12) Mouse mAb	Cell Signaling Technology	Cat.# 4696
Phospho-MEK1/2 (Ser217/221) (41G9) Rabbit mAb	Cell Signaling Technology	Cat.# 9154
MEK1/2 (L38C12) Mouse mAb	Cell Signaling Technology	Cat.# 4694
MEK1/2 (D1A5) Rabbit mAb	Cell Signaling Technology	Cat.# 8727
Cyclin B1 (V152) Mouse mAb	Cell Signaling Technology	Cat.# 4135
HA-Tag (C29F4) Rabbit mAb #3724	Cell Signaling Technology	Cat.# 3724
DYKDDDDK Tag (D6W5B) Rabbit mAb	Cell Signaling Technology	Cat.# 14793
GST (91G1) Rabbit mAb	Cell Signaling Technology	Cat.# 2625
Phospho-CDK Substrate Motif [(K/H)pSP] MultiMab Rabbit mAb	Cell Signaling Technology	Cat.# 9477
PTTG Antibody (DCS-280) Mouse mAb	Santa Cruz Biotechnology	Cat.# sc-56207
GST Antibody (B-14) Mouse mAb	Santa Cruz Biotechnology	Cat.# sc-138
MAD2 Antibody (17D10) Mouse mAb	Santa Cruz Biotechnology	Cat.# sc-47747
RIT1 Rabbit pAb	Abcam	Cat.# ab53720
p31comet Antibody, clone E29.19.14, Mouse mAb	EMD Millipore	Cat.# MABE451
MAD2 Rabbit pAb	Bethyl Laboratories	Cat. # A300-301A
β-Actin Mouse mAb	Sigma-Aldrich	Cat.# A2228
FLAG M2 Mouse mAb	Sigma-Aldrich	Cat.# F1804
Histidine Tagged Antibody, clone HIS.H8, Mouse mAb	Sigma-Aldrich	Cat.# 05-949
α-Tubulin Mouse mAb	Sigma-Aldrich	Cat.# T6199
C-MAD2 (157) Mouse mAb	[47]	
Rabbit IgG (H&L) Antibody DyLight™ 680 Conjugated, Goat polyclonal	Rockland Inc.	Cat.# 611-144-002
Mouse IgG (H&L) Antibody DyLight™ 800 Conjugated Goat Polyclonal	Rockland Inc.	Cat.# 610-145-002
Bacterial and Virus Strains		
BL21(DE3)	New England Biolabs	Cat.# C2527H
DH5α	McCormick Lab	N/A
Stbl3	McCormick Lab	N/A
Chemicals, Peptides, and Recombinant Proteins		
Nocodazole	Selleckchem	Cat.# S2775
Reversine	Selleckchem	Cat.# S7588
Dinaciclib	Selleckchem	Cat.# S2768
RO-3306	Selleckchem	Cat.# S7747
JNK-IN-8	Selleckchem	Cat.# S4901
CHIR-99021	Selleckchem	Cat.# S2924
TG003	Selleckchem	Cat.# S7320
Losmapimod	Selleckchem	Cat.# S7215

REAGENT or RESOURCE	SOURCE	IDENTIFIER
Antibodies		
Trametinib	Selleckchem	Cat.# S2673
MG132	Sigma-Aldrich	Cat.# M8699
Thymidine	Sigma-Aldrich	Cat.# T1895
ATP	Sigma-Aldrich	Cat.# A7699
Creatine Phosphate	Sigma-Aldrich	Cat.# 2380
GDP	Sigma-Aldrich	Cat.# G7127
GTPγS	Sigma-Aldrich	Cat.# G8634
MBP1 (SWYSYPPPQRAV)	GenScript	N/A
Control peptide (SYWPQRAPPSVY)	GenScript	N/A
RIT1 (202-216) peptide	GenScript	N/A
pS209 RIT1 (202-216) peptide	GenScript	N/A
Hexadimethrine bromide	Sigma-Aldrich	Cat.# 107689
Isopropyl β-D-1-thiogalactopyranoside (IPTG)	Sigma-Aldrich	Cat.# I5502
Protease Inhibitor Cocktail	Sigma-Aldrich	Cat.# P8849
TEV-Protease	Sigma-Aldrich	Cat.# T4455
Phosphatase Inhibitor Cocktail 1	Sigma-Aldrich	Cat.# P2850
Phosphatase Inhibitor Cocktail 2	Sigma-Aldrich	Cat.# P5726
Protease Inhibitor Cocktail (mammalian cell extracts)	Sigma-Aldrich	Cat.# P8340
ProLong Gold Antifade Mountant with DAPI	Invitrogen	Cat.# P36935
KaryoMAX Colcemid Solution in PBS	Thermo Fisher Scientific	Cat.# 15212012
GlutaMAX	Thermo Fisher Scientific	Cat.# 35050061
active CDK1/Cyclin B1	SignalChem	Cat.# C22-10G
Ubiquitin	Boston Biochem	Cat.# U-100H
UbcH10	Boston Biochem	Cat.# E2-650
Creatine phosphokinase	Sigma-Aldrich	Cat.# C7886
Critical Commercial Assays		
MycoAlert PLUS Mycoplasma Detection Kit	Lonza	Cat.# LT07-710
Subcellular Protein Fractionation Kit for Cultured Cells	Thermo Fisher Scientific	Cat.# 78840
NuPAGE 4-12% Bis-Tris Gel	Invitrogen	Cat.# NP0321BOX
NuPAGE Sample Loading Buffer	Invitrogen	Cat.# NP0007
Glutathione Sepharose 4B	Cytiva Life Sciences	Cat.# 17075605
ANTI-FLAG M2 Affinity Gel	EMD Millipore	Cat.# A2220
ZipTip with 0.6 μL C18 resin	Millipore	Cat.# ZTC18S008
Gateway LR Clonase II Enzyme Mix	Thermo Fisher Scientific	Cat.# 11791100
Gateway BP Clonase II Enzyme Mix	Thermo Fisher Scientific	Cat.# 11789100
Superdex 200 Increase 3.2/300 column	Cytiva Life Sciences	Cat.# 28990946
RESOURCE Q anion exchange chromatography column	Cytiva Life Sciences	Cat.# 17117701
HisTrap FF (1ml) column	Cytiva Life Sciences	Cat.# 17531901

REAGENT or RESOURCE	SOURCE	IDENTIFIER
Antibodies		
Superdex 75 Increase 10/300 GL column	Cytiva Life Sciences	Cat.# 29148721
Deposited Data		
Experimental Models: Cell Lines		
Human: HEK-293T	ATCC	Cat.# CRL-3216
Human: HeLa	ATCC	Cat.# CCL-2
HeLa RIT1 KO-1 (clone 1)	This paper	N/A
HeLa RIT1 KO-2 (clone 2)	This paper	N/A
Human: U2-OS	ATCC	Cat.# HTB-96
Human: HCT-116	ATCC	Cat.# CCL-247
Human: hTERT RPE-1	ATCC	Cat.# CRL-4000
hTERT RPE-1 RIT1 KO (three clonal lines)	This paper.	N/A
hTERT RPE-1 RIT1 WT (three clonal lines)	This paper.	N/A
Oligonucleotides		
SMARTpool: ON-TARGETplus RIT1	Horizon	N/A
ON-TARGETplus Non-targeting Control Pool	Horizon	Cat.# D-001810-10-05
Recombinant DNA		
psPAX2	gift from Didier Trono	Addgene plasmid #12260
pMD.2G	gift from Didier Trono	Addgene plasmid #12259
pDONR221	Invitrogen	Cat.# 12536017
pDEST566	gift from Dominic Esposito	Addgene plasmid #11517
pDEST527	gift from Dominic Esposito	Addgene plasmid #11518
pLenti6-H2B-mCherry	[48]	Addgene plasmid #89766
pSpCas9(BB)-2A-GFP (PX458)	[49]	Addgene plasmid #48138
PX458-sgRIT1-1	This paper	N/A
PX458-sgRIT1-2	This paper	N/A
pGEX-MAD2	This paper	N/A
pGEX-MAD2 ΔC	This paper	N/A
pGEX-MAD2 LL	This paper	N/A
pGEX-MAD2 V193N	This paper	N/A
pGEX-MAD2 L13A	This paper	N/A
pGEX-MAD2 ΔN15	This paper	N/A
pGEX-p31^{comet}	This paper	N/A
pGEX-RIT1	This paper	N/A
pGEX-RIT1 (*D. rerio*)	This paper	N/A
pGEX-RIC (*D. melanogaster*)	This paper	N/A
pGEX-RGL3 RBD	This paper	N/A
pGEX-CDC20 111-138	This paper	N/A
pDEST527-RIT1	This paper	N/A

REAGENT or RESOURCE	SOURCE	IDENTIFIER
Antibodies		
pDEST527-MAD2	This paper	N/A
pDEST527-MAD2 RQ	This paper	N/A
pDEST527-MAD2 (*D. rerio*)	This paper	N/A
pDEST527-MAD2 (*D. melanogaster*)	This paper	N/A
pDEST566-p31^{comet}	This paper	N/A
pDEST566-p31^{comet} ΔN	This paper	N/A
pDEST27-RIT1	This paper	N/A
pDEST27-RIT2	This paper	N/A
pDEST27-RIT1 ΔN	This paper	N/A
pDEST27-RIT1 ΔC	This paper	N/A
pDEST27-RIT1 ΔC5	This paper	N/A
pDEST27-RIT1 ΔC10	This paper	N/A
pDEST27-RIT1 ΔC15	This paper	N/A
pDEST27-RIT1 ΔC20	This paper	N/A
pDEST27-RIT1 Ct	This paper.	N/A
pDEST27-RIT1 GSL	This paper	N/A
pDEST27-RIT1/RIT2 Ct	This paper	N/A
pDEST27-RIT1 A57G	[11]	N/A
pDEST27-RIT1 A77P	[11]	N/A
pDEST27-RIT1 F82L	[11]	N/A
pDEST27-RIT1 M90I	[11]	N/A
pDEST27-RIT1 S209A	This paper	N/A
pDEST27-RIT1 S209D	This paper	N/A
pDEST27-RIT1 S209E	This paper	N/A
pDEST27-HRAS	[10]	N/A
pDEST27-NRAS	[10]	N/A
pDEST27-KRAS	[10]	N/A
pDEST27-RRAS	[10]	N/A
pDEST27-MRAS	[10]	N/A
pDEST27-TC21	[10]	N/A
pDEST27-RAP1	[10]	N/A
pDEST27-RAP2	[10]	N/A
pDEST27-RHEB	[10]	N/A
pDEST302-3xFLAG-EV	This paper	N/A
pDEST302-3xFLAG-RIT1	This paper	N/A
pDEST663-3xFLAG-EV	This paper	N/A
pDEST663-3xFLAG-RIT1	This paper	N/A

REAGENT or RESOURCE	SOURCE	IDENTIFIER
Antibodies		
pDEST663-3xFLAG-RIT1 M90I	This paper	N/A
pDEST663-3xFLAG-RIT1 M90I/S209A	This paper	N/A
pDEST663-3xFLAG-RIT1 M90I/S209A	This paper	N/A
pDEST663-3xFLAG-RIT1 M90I/S209A	This paper	N/A
pDEST686-3xFLAG-mNeonGreen RIT1	This paper	N/A
pCDNA3-HA-MAD2	This paper.	N/A
pCDNA3-HA-MAD2 S295A	This paper	N/A
pCDNA3-HA-MAD2 S295D	This paper	N/A
Software and Algorithms		
Prism 8	GraphPad	https://www.graphpad.com/
ZEN 2.1 Blue	Zeiss	https://www.zeiss.com
Fiji	[50]	https://imagej.net/Fiji
Skyline v20	[51]	https://skyline.ms
Excel	Microsoft	https://www.microsoft.com